A system for measuring the pattern of cell divisions in *Caenorhabditis elegans* embryos

Shugo Hamahashi

School of Science for Open and Environmental Systems

Graduate School of Science and Technology

Keio University

A dissertation submitted for the degree of

Doctor of Philosophy

2005

Summary

The pattern of cell divisions provides crucial information to understand the mechanism of development in multicellular organisms. The pattern of cell divisions holds the position and time of individual cell and relationships between mother cells and their daughter cells. Many analyses of development often compare patterns of cell divisions, where differences of timings or orientations of cell divisions and/or positions of cells among wild-type and mutant embryos are investigated. The scales of these analyses are getting larger, so that the importance of objectivity and productivity in measuring the pattern of cell divisions are getting more critical. However, the patterns of cell divisions in *Caenorhabditis elegans* embryo has been manually measured by direct observation with a microscope, so that the objectivity and productivity of the measurement has been seriously low. Therefore, I developed a system that objectively and productively measures a pattern of cell divisions of *C. elegans* embryo. This system first automatically detects nuclei in a set of images recorded by the 4-dimensional differential interference contrast (DIC) microscope system using nuclear regions that are image regions detecting nuclei in DIC microscope images. The nuclear regions are produced using the difference in image textures between the nucleus and the cytoplasm distinguished by local image entropy. This system then automatically identifies the 3-dimensional (3D) region of individual nuclei by grouping nuclear regions, tracks these 3D regions, and outputs the tracking trajectory. This tracking trajectory is the measured pattern of cell divisions. This system measures a pattern of cell divisions from fertilization to the onset of gastrulation of a *C. elegans* embryo. This system is the first embodiment that enables the objective and productive measurement of the pattern of cell divisions, which would greatly contribute to the future studies of development in multicellular organism.

Acknowledgments

I am sincerely grateful to my advisor, Dr. Shuichi Onami, who provided unfailing guidance and invaluable advices and comments. I am greatly indebted to Dr. Hideharu Amano for his support and helpful comments. I am grateful to Dr. Yuichiro Anzai, Dr. Yoshio Ohno and Dr. Motonori Hoshi for helpful comments. I would like to thank Dr. Hiroaki Kitano for his helpful comments and discussions. I would like to thank Dr. Mario Tokoro who gave me an opportunity to study in the field of computational biology.

I am grateful to Dr. Koji Kyoda who helped the software development and provided helpful comments and discussions. I would like to thank Mineo Morohashi and Dr. Akatsuki Kimura for their helpful comments and discussions. I would like to thank Mitsuru Urai, Takeshi Umezawa, Yasunori Osana, Dr. Mitsunobu Kunishi and all members in the Onami, Anzai and Amano laboratories for their supports. I would like to thank Dr. Michimune Kohno and Dr. Takahiro Sasaki for helpful advises. I would like to thank Masato Ito, Kiichi Kitajima, Yuichiro Maeda, Kazuhiro Shitama, Shokei Suda and Yoshiteru Takeshima for their continued encouragements.

I would like to thank Dr. Kenneth Kemphues for providing the *par-1* (KK288) mutant. I would like to thank Dr. Julie Ahringer, Cambridge University Technical Services Limited and UK MRC Human Genome Mapping Project Resource Center, for providing *C. elegans* chromosome 1 RNAi library.

Finally, I would like to thank my parents, Masakuni and Nobue, for their continued encouragement and support. I would like to thank my brother, Taizo, for his help and encouragement.

Shugo Hamahashi

December 2005

Table of contents

Summary 1
Acknowledgments 2
Table of contents 3
List of Figures 4
List of Tables 5
List of Abbreviations 6
Publications arising from this work 7
Chapter 1 Introduction 8
Chapter 2 Basic system: a system detecting the nuclei 13
2.1 Introduction 13
2.2 Results 14
2.3 Discussion 29
2.4 Summary 35
Methods 35
Chapter 3 Main system: a system measuring the pattern of cell divisions 37
3.1 Introduction 37
3.2 Results 38
3.3 Discussion 53
3.4 Summary 57
Methods 57
Chapter 4 Derivative system: a system measuring the spindle orientation 59
4.1 Introduction 59
4.2 Results 60
4.3 Discussion 66
4.4 Summary 67
Methods 67
Chapter 5 Conclusion 69
5.1 Summary of results 69
5.2 Prospects 70
References 72

List of Figures

Figure 1.1 Cell division pattern 8
Figure 2.1 Overview of 4-dimensional differential interference contrast microscope images of *Caenorhabditis elegans embryo* 14
Figure 2.2 Effect of window size and threshold value on production of low-entropy regions ..16
Figure 2.3 Values of local image entropy and Yasuda *et al.*'s measure 21
Figure 2.4 Low-entropy regions of different focal planes and different time points 23
Figure 2.5 Overview of forward and backward trackings....26
Figure 2.6 Low-entropy regions in a *par-1* embryo....31
Figure 2.7 Low-entropy regions in a *tba-2(RNAi)* embryo....32
Figure 3.1 Overview of the system and the visualization software 39
Figure 3.2 Snapshot of graphical user interface in the nuclear detection module 40
Figure 3.3 Low-entropy regions produced by the local image entropy 41
Figure 3.4 Nuclear regions after the removal of non-nuclear regions 42
Figure 3.5 Nuclear regions separately produced by the nuclear detection module....43
Figure 3.6 Step 1 and step 2 in the nuclear lineaging module 45
Figure 3.7 Falsely merged nuclear region produced by the nuclear detection module....46
Figure 3.8 Overview of the error-correction module....48
Figure 3.9 Images of wild-type and *par-1* embryos in 2- and 4-cell stages....52
Figure 4.1 Detection of spindles in a *Caenorhabditis elegans* embryo 60
Figure 4.2 Orientation of nuclear regions of spindle 61
Figure 4.3 Spindle orientations in a wild-type embryo....62
Figure 4.4 Spindle orientations in a *par-3(RNAi)* embryo....64
Figure 4.5 Time-transitions of spindle orientations 65

List of Tables

Table 2.1 Discriminability and computation time of widely-used texture measures.....19
Table 2.2 Performance of nuclear detection by low-entropy regions and those selected by forward and backward trackings.....24
Table 2.3 Number of image sets for which advanced trackings detected nuclei with perfect sensitivity.....24
Table 2.4 Specificity of nuclear detection by low-entropy regions selected by advanced forward and backward trackings.....28
Table 3.1 Required time for measuring a cell division pattern of wild-type embryo from one- to 24-cell stages 50
Table 3.2 A part of a cell division pattern from 2- to 3-cell stages of a wild-type embryo 50
Table 3.3 Verification of measured cell division patterns from one- to 24-cell stages of wild-type embryos.....51
Table 3.4 Time periods between cell stages in wild-type and *par-1* embryos.....52
Table 3.5 Comparison of distance between nuclei of 4-cell stage in wild-type and *par-1* embryos.....53

List of Abbreviations

2D	two-dimensional
3D	three-dimensional
4D	four-dimensional
CDP	cell division pattern
DIC	differential interference contrast
ECM	error-correction module
GUI	graphical user interface
NDM	nuclear detection module
NDS	nuclear detection system
NLM	nuclear lineaging module
PC	personal computer
RAM	random access memory
RNA	ribonucleic acid
RNAi	RNA interference

Publications arising from this work

Onami, S., Hamahashi, S., Nagasaki, M., Miyano, S. and Kitano, H. Automatic acquisition of cell lineage through 4D microscopy and analysis of early *C. elegans* embryos. In *Foundations of Systems Biology*. (Ed) Kitano, H., MIT Press, Cambridge, Massachusetts, 39-55, 2001.

Hamahashi, S., Onami, S. and Kitano, H. Detection of nuclei in 4D Nomarski DIC microscope images of early *Caenorhabditis elegans* embryos using local image entropy and object tracking. *BMC Bioinformatics* 6, 125, 2005.

Hamahashi, S. and Onami, S. Objective measurement of spindle orientation in early *Caenorhabditis elegans* embryo. *Genome Informatics* 16, 86-93, 2005.

Hamahashi, S., Kitano, H. and Onami, S. A system for identification of cell division patterns in early embryogenesis of *Caenorhabditis elegans* using image processing and object tracking. *Institute of Electronics, Information and Communication Engineers*, 2006, (accepted).

Chapter 1 Introduction

The pattern of cell divisions is a crucial piece of information in studies of development in multicellular organisms (hereafter a pattern of cell divisions is called a *cell division pattern (CDP)*). CDP holds timings and orientation of cell divisions and relationships between mother cells and their daughter cells in terms of cell lineage information (Figure 1.1). CDP is described by following cells during embryogenesis in individual organisms (Sulston *et al.*, 1983; reviewed by Stern and Fraser, 2001; Chisholm, 2002). A fertilized egg—a single cell—develops into a multicellular organism through many spatially and temporally dynamic cellular activities, including cell division, cell migration, cell differentiation and cell death. In *Caenorhabditis elegans*, CDPs and cell fates are correlated (Sulston *et al.*, 1983), where mutations affect CDPs such as timings and orientations of cell divisions. CDP is greatly contributing to understanding the mechanisms underlying the development of the organism.

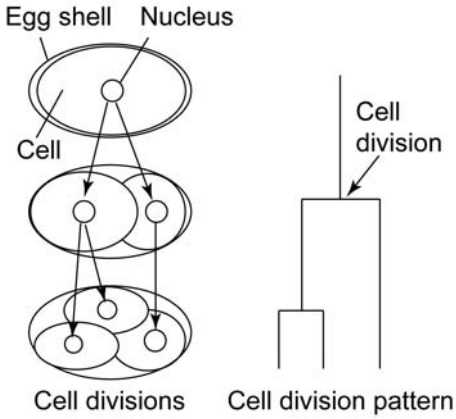

Figure 1.1 Cell division pattern. A conceptual schematic diagram is shown to the left. The cell division pattern corresponding to the conceptual schematic diagram is shown to the right.

CDP is mostly the same as the cell lineage but more informative about the positions of cells. The cell lineage is described with timings and orientations of cell divisions and relationships between mother cells and their daughter cells (Sulston *et al.*, 1983). The orientations of cell divisions are determined using positions of nuclei in cells, but positions of nuclei themselves are not described in the cell lineage. Because my system presented in this dissertation measures both the cell lineage and the positions of nuclei, I use the term "CDP" to call information holding both of them instead of the term "cell lineage".

I chose *C. elegans* as a model in my work because of the importance of the animal in biology. *C. elegans* is the simplest multicellular organism that has been most extensively studied in biology (Wood, 1988; Riddle *et al.*, 1997). The total number of cells is only about a thousand (Wood, 1988). In spite of the simplicity in number of cells, *C. elegans* has differentiated cells, such as an epidermis, intestine, excretory system, and nerve and muscle cells, which makes this animal an ideal model for anatomically analyzing the development of multicellular organisms. Besides, *C. elegans* is an ideal model for genetic analysis. *C. elegans* has a short life cycle; the embryogenesis takes about 12 hours and the generation cycle takes about 3 days (Wood, 1988). Thus, the animal is suited for genetic experiments. Functions of genes are conserved from *C. elegans* to mammals (Yuan *et al.*, 1993; Hengartner and Horvitz, 1994), which makes the genetic analysis of this animal suggestive for understanding higher multicellular organisms. These features make *C. elegans* an excellent model for study in biology. Consequently, I considered that the animal is suited for a model in my work.

CDP has been manually measured in *C. elegans*. Timings and orientations of cell divisions are manually identified by human recognition, where the orientations are determined using positions of nuclei because the nucleus is generally positioned at the center of a cell and is the most noticeable organelle in a cell (Sulston *et al.*, 1983). The positions of nuclei are measured by direct observation or using recorded images with a Nomarski differential interference contrast (DIC) light microscope (hereafter this microscope is called a *DIC microscope*) (Nomarski and Weill, 1955). The four-dimensional (4D) DIC microscope (Hird and White, 1993; Thomas *et al.*, 1996) is usually used to automatically record a set of images in multiple focal planes and at multiple time points for a specimen (hereafter a set of these images is called a *set of 4D DIC microscope images*). Nuclei move 3-dimensionally within a time interval of a set of 4D DIC microscope images. To measure CDP, individual nuclei at adjacent time points are identified and are followed, and the relationships between mother nuclei and their daughter nuclei are identified and are followed by eye observation.

The objectivity and productivity in measuring CDP have been low because the measurement has been mostly a manual process as described above. Analyses of development often compare CDPs (such as timings, orientations of cell divisions and/or positions of nuclei) among wild-type and mutant embryos (Kemphues *et al.*, 1988), where the high objectivity in the measurements is an important matter. *C. elegans* has about twenty thousand genes (The *C. elegans* Sequencing Consortium, 1998). The recent establishment of RNA interference (RNAi) has enabled us to make each of large numbers of genes silent (Fire *et al.*, 1998). Using such a benefit of RNAi, large-scale functional genomic analyses have been initiated (Fraser *et al.*, 2000; Gönczy *et al.*, 2000;

Sönnichsen *et al.*, 2005). To investigate the functions of genes using CDPs in such a large-scale manner, the high productivity of the measurement of CDP is an important matter, too.

To help the manual measurement of CDP in *C. elegans*, two computer-aided systems have been developed, namely SIMI BioCell (Schnabel *et al.*, 1997) and 3D-DIASemb (Heid *et al.*, 2002). SIMI BioCell has a graphical user interface (GUI) that can display a set of 4D DIC microscope images, help identifying the positions of nuclei, and record these identified positions. 3D-DIASemb is similar to SIMI BioCell but can also record and display the perimeters of nuclei and cells. Although both of these systems help greatly to follow nuclei through time points in a set of 4D DIC microscope images, detecting and following nuclei are manually processed, where the positions of nuclei are determined by human recognition and those manual processes are time-consuming and labor-intensive. Therefore, the objectivity and productivity in measuring CDP are low in these systems.

To increase the objectivity and productivity in measuring CDP, automating the processes in the measurement will be an effective strategy. If detecting nuclei is automated, the positions of nuclei are expected to be measured without human subjectivity and without time and labor, i.e. positions of nuclei will be measured objectively and productively. Similarly, if following nuclei is automated, the same nucleus in adjacent time points (in a set of 4D DIC microscope images) is identified objectively and productively. Yasuda *et al.* attempted to develop such an automated system (Yasuda *et al.*, 1999). Yasuda *et al.*'s system automatically detects and follows nuclei in a set of 4D DIC microscope images. However, because their system can not detect nuclei that are in the process of cell division, their system can not measure the timing of cell division which is an important element of CDP. Furthermore, their system needs laborious hand-tuning of system's parameters every time a new set of 4D DIC microscope images is applied, which is a serious problem in productivity of the measurement of CDP when the system is applied to large-scale analyses (Fraser *et al.*, 2000; Gönczy *et al.*, 2000; Sönnichsen *et al.*, 2005). Besides, the maximum cell stage of their measured CDP is limited under eight-cell stage. Consequently, their system requires marked improvement before it becomes applicable to analyses that use CDPs.

In this dissertation, I present a system that objectively and productively measures a CDP in a set of 4D DIC microscope images of *C. elegans* embryo. Actually, I present three systems that I have developed during my work (Hamahashi and Onami, 2005; Hamahashi *et al.*, 2005; Hamahashi *et al.*, 2006). The first system is a basic system that detects nuclei in *C. elegans* embryo. The second system is the main system that measures CDP in *C. elegans* embryo. The third system is a derivative system that measures spindle orientations in *C. elegans* embryo. The strategy to increase the

objectivity and productivity of the measurement in these systems is the automation of the measurements.

Basic system: The first system attained the highly objective and productive detection of nuclei in a set of 4D DIC microscope images of *C. elegans*. This system automatically detects nuclei using a difference in image textures between the nucleus and the cytoplasm in DIC microscope images. The difference is distinguished by local image entropy (Handmann *et al.*, 2000) which makes the system applicable to different sets of 4D DIC microscope images without the need of hand-tuning of system's parameters. The system produces image regions that detect nuclei (hereafter an image region that detect a nucleus is called a *nuclear region*) but also produces image regions that do not detect nuclei (they detect such as the boundaries between cells and the spaces between the embryo and the eggshell). This system automatically selects nuclear regions from produced regions using an object-tracking algorithm (Geerts *et al.*, 1987; Lee *et al.*, 1991; Awasthi *et al.*, 1994). The object-tracking algorithm allows selecting nuclear regions detecting nuclei that are both in and not in the process of cell division, which makes this system possible to detect nuclei that are in the process of cell division. Details about this system are explained in Chapter 2.

Main system: The second system attained the highly objective and productive measurement of CDP in *C. elegans*. This system is the main system to measure CDP. This system first produces nuclear regions from a set of 4D DIC microscope images using the basic system. Then, this system identifies the 3-dimensional (3D) region of each nucleus by a unit that groups nuclear regions detecting the same nucleus (explained in section 3.2.3). Finally, this system tracks units along a time line and outputs a tracking trajectory that is the measured CDP. If a unit groups inappropriate nuclear regions, this system detects the unit and corrects it (such as cuts and/or merges nuclear regions) to make a new unit that groups modified nuclear regions (explained in section 3.2.4). If this system inappropriately tracks units (nuclei detected by a tracker and a tracked units are different), this system detects this failure and corrects it (explained in section 3.2.4). This system allows almost automatically measuring a CDP in a *C. elegans* embryo from one- to 24-cell stages, where the objectivity and productivity of the measurement are high.

Derivative system: The third system attained the objective and productive measurement of spindle orientation during second cell divisions in *C. elegans* embryo. This system is a derivative system that is developed based upon the main system, which demonstrates the applicability of the main system. Spindle orientations are often measured in many analyses of development (Kemphues *et al.*, 1988; Cheng *et al.*, 1995; Watts *et al.*, 1996), where the spindle orientation correlates with the orientation of cell division and is suggestive for understanding the mechanism of development. The

objectivity and productivity are the important matters in these analyses. This system first automatically detects spindle using nuclear region produced by a module (the nuclear detection module explained in section 3.2.2) in the main system, where the objectivity and productivity in detecting spindles are high. Then, this system measures the spindle orientation using the regression line (Montgomery and Peck, 1982), where the objectivity and productivity in acquiring the orientations are high. Consequently, this system objectively and productively measures the spindle orientation in *C. elegans* embryo.

Chapter 2 Basic system: a system detecting the nuclei

2.1 Introduction

Yasuda *et al*. attempted to automate nuclear detection (Yasuda *et al.*, 1999). Their system detected nuclei from two- to eight-cell stages in a specific set of 4D DIC microscope images using several edge detection operators (Prewitt, 1970; Kirsch, 1971). However, their system requires laborious hand-tuning of parameters every time a new set of 4D DIC microscope images was applied, because the edge detection operators were very sensitive to differences in image quality (e.g., brightness, contrast) among sets of images; the differences could be controlled but not eliminated (see section 2.2.4 and section 2.3.1). In addition, their system was not able to detect the nucleus that was in the process of cell division, because their detection of nucleus relied on the shape of nucleus being round (and therefore not in the process of division).

In this chapter, I present a system that I have developed to automate the detection of nuclei in a set of 4D DIC microscope images of *C. elegans* embryo (Hamahashi *et al.*, 2005). In this system, local image entropy is used to produce regions of the images that have the image texture of the nucleus. From these regions, those that actually detect nuclei are manually selected at the first and last time points of the image set, and an object-tracking algorithm (Geerts *et al.*, 1987; Lee *et al.*, 1991; Awasthi *et al.*, 1994) then selects regions that detect nuclei in between the first and last time points. The use of local image entropy makes the system applicable to multiple image sets without the need to tune parameters. The use of an object-tracking algorithm enables the system to detect nuclei in the process of cell division. The system detected nuclei with high sensitivity and specificity from the one- to 24-cell stages.

2.2 Results

2.2.1 Appearance of nuclei in a set of 4D DIC microscope images

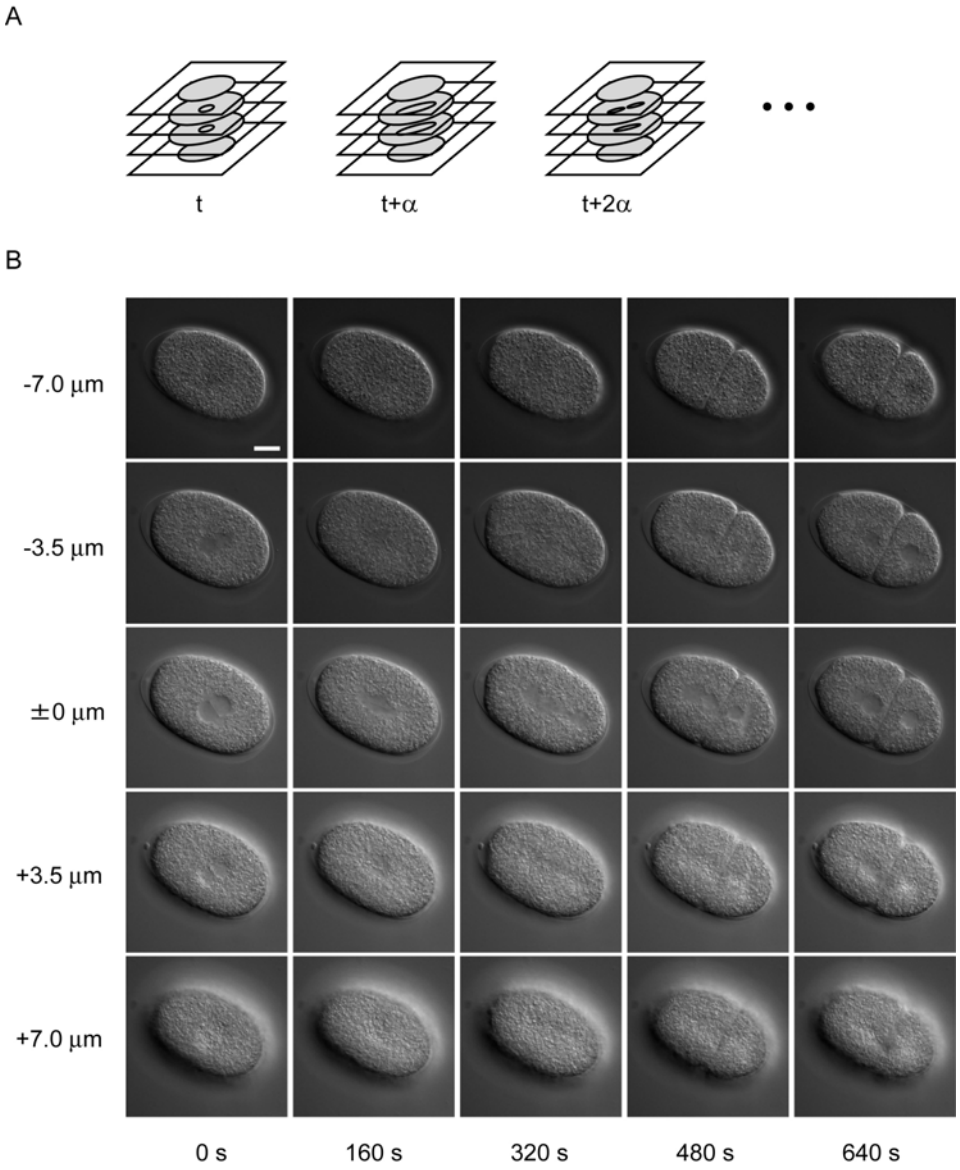

Figure 2.1 Overview of 4-dimensional differential interference contrast microscope images of *Caenorhabditis elegans* embryo. (A) Schematic of 4-dimensional (4D) differential interference contrast (DIC) microscope images. Digital images of a developing embryo were recorded in multiple focal planes and a set of multifocal images was recorded with a fixed time interval, α. (B) Example of 4D DIC microscope images of a *C. elegans* embryo. Each column shows multifocal images recorded at a specific time point, with 3.5 µm between two focal planes. Each row shows time-lapse images recorded in a specific focal plane with 160 s between two time points. Bar is 10 µm.

The appearance of nuclei of *C. elegans* embryos in a set of 4D DIC microscope images (Figure 2.1) varies among different focus levels and different developmental stages. The nucleus appears as a smooth, round region in the center of the cell, the cytoplasm of which appears as a rough region at all developmental stages. The boundary of the nucleus is apparent when the focus level is close to the level of the center of the nucleus (0 μm, 0 s in Figure 2.1B). As the focus level becomes higher or lower, the nucleus becomes smaller, reflecting the 3D shape of the nucleus and the boundary of the nucleus becomes blurred (–3.5 μm and +3.5 μm in Figure 2.1B). The nucleus becomes invisible when the focus level goes beyond the level of the upper or lower end of the nucleus (–7.0 μm and +7.0 μm in Figure 2.1B). As the embryo develops, the number of cells in the embryo increases through repeated cell divisions, each of which produces two daughter cells from a single mother cell. When cell division begins, the nucleus begins to elongate and the boundary of the nucleus becomes blurred (160 s in Figure 2.1B). As cell division progresses, the nucleus continues to elongate (320 s in Figure 2.1B). The elongated nucleus is fragmented into several pieces (480 s in Figure 2.1B), which then form daughter nuclei in two daughter cells (640 s in Figure 2.1B). The size of the nuclei gradually decreases as the embryo develops and the number of nuclei increases (8 μm in diameter at the one-cell stage and 5 μm at the 24-cell stage). Although the appearance of the nuclei in the images varies among different focal planes and different developmental stages, a smooth image texture is a common feature of the appearance of nuclei.

2.2.2 Detection of nuclei using regions of low local image entropy

To detect nuclei in the 4D DIC microscope images, I used a common feature of nuclei in the images, that is, their smooth image texture (see previous section, Figure 2.1B). To quantify the smoothness of image texture in various regions of an image, I used local image entropy (Handmann *et al.*, 2000), which computes the image entropy (Pratt, 1991) of a small area surrounding a point of interest in an image. Image entropy represents the smoothness of image texture; its value becomes high when the texture is rough and low when the texture is smooth. Because smooth image texture is a common feature of the appearance of nuclei in 4D DIC microscope images, I expected local image entropy to be lower in the nuclei than in the cytoplasm. An important feature of image entropy is low sensitivity to differences in image quality, particularly in terms of the brightness of the image. Therefore, I expected that local image entropy would quantify the smoothness of image texture in multiple images in a manner that was not sensitive to differences in quality among images. (The validity of choosing image entropy from widely-used texture measures is evaluated in section 2.2.3.)

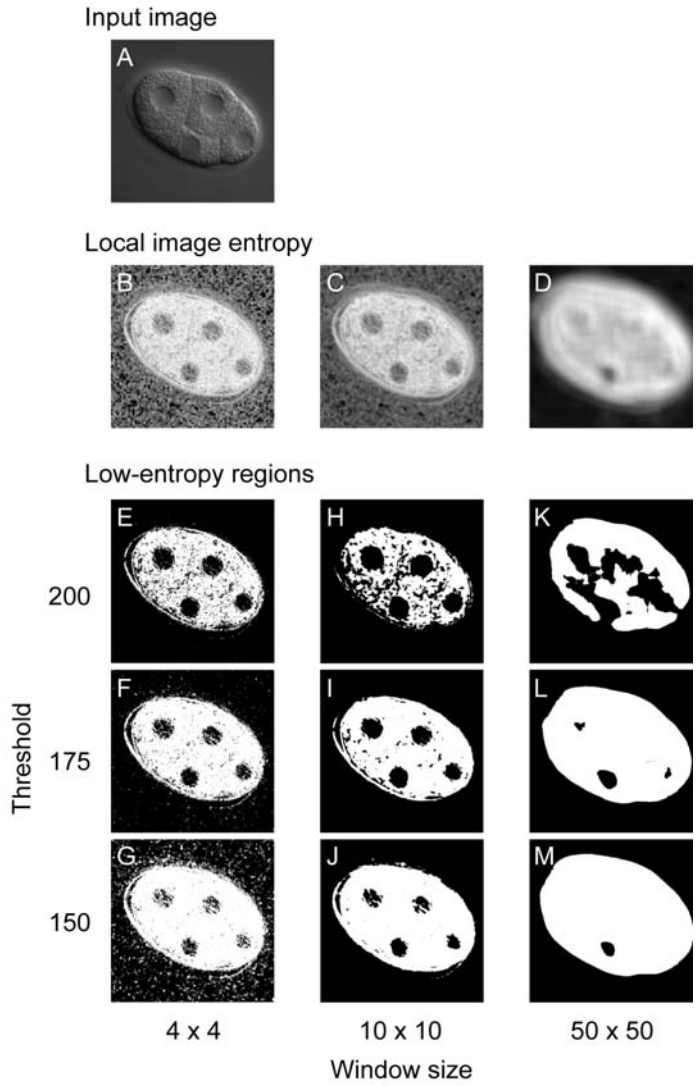

Figure 2.2 Effect of window size and threshold value on production of low-entropy regions. (A) Input image. Low-entropy regions were produced from an image of a four-cell-stage embryo using various window sizes and threshold values. (B–D) Effect of window size on image conversion using local image entropy. The input image was applied to the image conversion using window sizes of 4 × 4 (B), 10 × 10 (C), and 50 × 50 (D) pixels. Darker colors represent lower local image entropies. (E–M) Effect of window size and threshold value on low-entropy regions. Low-entropy regions (black) were produced using threshold values of 200 (E, H, K), 175 (F, I, L), or 150 (G, J, M) from the images resulting from the image conversion, using window sizes of 4 × 4 (E–G), 10 × 10 (H–J) or 50 × 50 (K–M) pixels. A window of 10 × 10 pixels corresponds to that of 1 μm × 1 μm.

I defined an image conversion using local image entropy as follows. Let $[x_{ij}]$ be the matrix representing a digitized input image. Then the result of image conversion using local image entropy in an $X \times Y$ pixel window is an image $[y_{ij}]$, where the value of y_{ij} equals the entropy of the input image lying in the $X \times Y$ pixel window W_{ij} whose top left is x_{ij}. The image entropy is $y_{ij} = -\sum_{k=0}^{N-1} P(k) \log_2 P(k)$, where N is the number of gray levels and $P(k)$ is the probability of occurrence of gray level k in W_{ij}. Because of the presence of the window, the number of columns and rows of $[y_{ij}]$ is smaller than those of $[x_{ij}]$ by $X - 1$ and $Y - 1$, respectively.

To determine whether local image entropy could effectively distinguish nuclei from cytoplasm in 4D DIC microscope images, I converted the images using various window sizes (from 2 × 2 to 50 × 50 pixels, results for 4 × 4, 10 × 10 and 50 × 50 pixels are shown in Figure 2.2). As expected, local image entropy was lower (darker) in the nuclei than in the cytoplasm (e.g., 10 × 10 window size in Figure 2.2). When I used a large (50 × 50) window, the difference in local image entropy between nuclei and cytoplasm became smaller. When I used a small (4 × 4) window, high-entropy spots (bright spots) appeared throughout the images. These results indicate that local image entropy effectively distinguishes nuclei from cytoplasm in 4D DIC microscope images. For images prepared in my experiments, 10 × 10 pixels (1 μm × 1 μm) appeared likely to be the optimal size of the window.

2.2.3 Evaluation of choosing image entropy from widely-used texture measures

There is a huge body of literature on texture analysis (Pratt, 1991; Tuceryan and Jain, 1998; Jahne *et al.*, 1999). To evaluate the validity of choosing image entropy from many texture measures, I investigated 25 widely-used texture measures selected from all four texture analysis methods categorized by Tuceryan and Jain (Tuceryan and Jain, 1998). The investigated texture measures are listed as follows:

A. Statistical methods
    a. First-order statistics
        1. Mean
        2. Standard deviation
        3. Skewness
        4. Kurtosis
        5. Energy
        6. Entropy
    b. Second-order statistics
        1. Co-occurrence: energy

2. Co-occurrence: entropy
3. Co-occurrence: contrast
4. Co-occurrence: homogeneity
5. Co-occurrence: correlation
6. autocorrelation

B. Geometrical methods
    1. Voronoi tessellation features
    2. Structural methods

C. Model based methods
    1. Markov random fields

D. Signal processing methods
    a. Spatial domain filters
        1. Laplacian operator
        2. Kirsch operator
        3. Prewitt operator
        4. Moment M00
        5. Moment M01
        6. Moment M02
        7. Moment M10
        8. Moment M11
        9. Moment M20
    b. Fourier domain filtering
        1. Radial features of power spectrum

For the evaluation of the performance of each measure, I implemented them in accordance with methods given in the literature (Pratt, 1991; Tuceryan and Jain, 1998; Jahne *et al.*, 1999) and applied them to my DIC microscope images of *C. elegans* embryos. The discriminability in image textures between the nucleus and the cytoplasm for each texture measure was judged using thresholding (Otsu, 1979) in which the value of each texture measure was binarized by its optimized threshold. The computation time for each texture measure was recorded. I did not implement the Geometrical methods measures, because my DIC microscope images were not composed of texture elements (Tuceryan and Jain, 1998).

Of the resulting 23 measures, 11 measures discriminated between nucleus and cytoplasm in my DIC microscope images of a *C. elegans* embryo (standard deviation; energy; entropy; co-occurrence: energy; co-occurrence: entropy; co-occurrence: homogeneity; co-occurrence: correlation; Markov

random field; Kirsch operator; Prewitt operator; and Fourier domain filtering). I concluded that, among these 11 measures, entropy provided the best performance for the NDS, as follows.

Entropy was better than the four second-order statistics measures (co-occurrence: energy; co-occurrence: entropy; co-occurrence: homogeneity; co-occurrence: correlation) and the Fourier domain filtering measure in terms of computation time. The computation time was at least 6.5 times longer than that of entropy in the case of these second-order statistics measures, and more than 200 times longer in the case of the Fourier domain filtering measure (Table 2.1). A shorter computation time is preferred in my system because my system was developed for detecting nuclei in 4D DIC microscope images of *C. elegans* embryos. A set of my 4D DIC microscope images usually consists of more than 6720 images from the one- to 24-cell stages.

Table 2.1 Discriminability and computation time of widely-used texture measures

Texture measure	Discriminability	Computation Time
Statistical methods		
first-order statistics		
mean	N	2.23
standard deviation	Y	3.01
skewness	N	3.84
kurtosis	N	4.07
energy	Y	2.19
entropy	Y	2.53
second-order statistics		
co-occurrence: energy	Y	14.60
co-occurrence: entropy	Y	16.50
co-occurrence: contrast	N	16.28
co-occurrence: homogeneity	Y	16.18
co-occurrence: correlation	Y	35.88
autocorrelation	N	16.30
Geometrical methods		
Voronoi tessellation features	N	N/A
Structural methods	N	N/A
Model based methods		
Markov random fields	Y	5.20
Signal processing methods		
spatial domain filters		
Laplacian operator	N	0.34
Kirsch operator	Y	1.22
Prewitt operator	Y	1.26
Moment M00	N	0.40
Moment M01	N	0.40
Moment M02	N	0.40
Moment M10	N	0.41
Moment M11	N	0.40
Moment M20	N	0.41
Fourier domain filtering		
radial features of power spectrum	Y	545.81

"Y" and "N" mean "discriminable" and "not discriminable" respectively. Computation times were measured by a PC which used a 3.2 GHz Intel Pentium 4 processor with HT Technology and 2 GB of SDRAM memory. All programs were written in a programming language C++.

Entropy was better than the two spatial domain filters (Kirsch operator and Prewitt operator) and the Markov random field in terms of sensitivity to differences in image quality (see section 2.2.4 and section 2.3.1). For the Markov random field, in more than 10 different DIC microscope images of *C. elegans* embryos, I tried but could not find a set of parameters with which the measure successfully discriminated the image textures between the nucleus and the cytoplasm.

Entropy was better than the two first-order statistics measures (standard deviation and energy) because entropy discriminated the image textures between the nucleus and the cytoplasm more clearly than did these two measures. Standard deviation, like entropy, is a texture measure widely-used to quantify the smoothness of image texture. In my test images, the standard deviation in the cytoplasmic region varied widely, and many small regions in the cytoplasm had standard deviations as small as in the nucleus. This wide variation in standard deviation in the cytoplasmic region may come from the dependency of standard deviation on actual pixel values in texture. Entropy does not depend on actual values in texture, but it does depend on the smoothness of texture. Energy discriminated between nucleus and cytoplasm far more clearly than did standard deviation. However, the difference in energy between the nucleus and cytoplasm was smaller than the difference in entropy.

2.2.4 Sensitivities to the image quality of local image entropy and Yasuda *et al.*'s measure

I investigated whether local image entropy is less sensitive to image quality than Yasuda *et al.*'s measure, because less sensitivity is preferred to eliminate a laborious hand-tuning of system's parameters. Yasuda *et al.*'s system (Yasuda *et al.*, 1999) used a combination of edge-detection operator (the Kirsch or the Prewitt operators) and the blur filter to detect nuclei from DIC microscope images; the combination of the edge-detection operator and the blue filter was the Yasuda *et al.*'s measure. To investigate the sensitivities to the image quality of local image entropy and Yasuda *et al.*'s measure, I used both local image entropy and Yasuda *et al.*'s measure and quantified the smoothness of image texture (Figure 2.3).

The gradient of Yasuda *et al.*'s measure at the boundary between nucleus and cytoplasm was easier than that of local image entropy (Figure 2.3). This result indicates that the nuclear detection using Yasuda *et al.*'s measure is more sensitive to the differences in image quality.

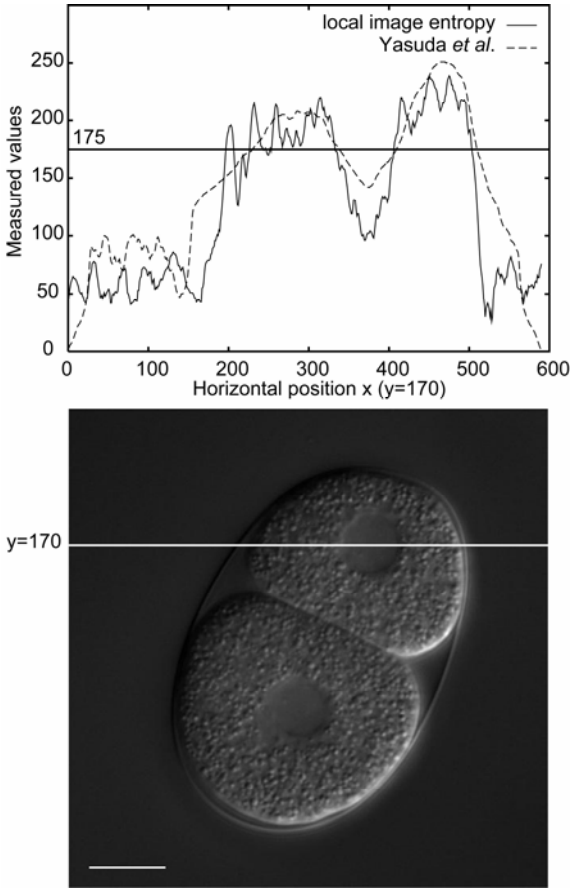

Figure 2.3 Values of local image entropy and Yasuda *et al.*'s measure. The upper figure shows values measured by local image entropy and Yasuda *et al.*'s measure. 175 is a threshold value to binarize the texture measures; the produced regions will consist of the positions having larger values than the threshold value. The horizontal position in the upper figure corresponds to the horizontal position in the lower picture of y = 170. In the upper figure, the solid line shows the values of local image entropy and the broken line shows the values obtained by our earlier system (Yasuda *et al.*, 1999). Bar is 10 μm.

2.2.5 Nuclear detection using low-entropy regions

To detect nuclei, I produced *low-entropy regions* (Figure 2.2E–M) applying thresholding (Otsu, 1979) to the images resulted from the image conversion of local image entropy. The low-entropy regions were produced as follows: neighboring pixels whose local image entropy was lower than the threshold were grouped, and the resulting group was defined as a low-entropy region. As expected, many of these low-entropy regions corresponded to nuclei in the original images, whereas the size and number of the regions depended on the threshold value. The shapes of the low-entropy regions approximated those of corresponding nuclei when the threshold value was set to 175 (Figure 2.2F, I, L). As the threshold value decreased, the regions became smaller and more fragmented (Figure 2.2G, J, M). As the threshold value increased, the regions became larger and more aggregated (Figure 2.2E,

H, K). These results indicate that low-entropy regions can be used to detect nuclei in 4D DIC microscope images. For images prepared in my experiments, 175 was likely to be the optimal threshold value. In addition to the low-entropy regions that corresponded to nuclei, many low-entropy regions were produced that did not correspond to nuclei. These low-entropy regions corresponded to regions that have similar (smooth) image textures to that of the nucleus, such as the boundaries between cells and the spaces between the embryo and the eggshell.

I evaluated the performance of nuclear detection in a set of 4D DIC microscope images by using low-entropy regions. For the evaluation, I produced low-entropy regions from five sets of images of *C. elegans* embryos using a 10 × 10 pixel window and a threshold value of 175 (Figure 2.4). Each set of images consisted of 10,080 images (56 focal planes × 180 time points = 10,080 images). I then calculated the sensitivity and specificity as measures of performance.

Sensitivity was defined as the ratio of the sum of the number of nuclei detected at each time point to the sum of the number of nuclei existing at each time point. A nucleus was considered to be "detected" at a specific time point when it was detected by at least one low-entropy region at any focal plane at this specific time point. This definition of sensitivity is reasonable because of the difficulty in specifying the number of low-entropy regions that are expected to detect a given nucleus. The following three factors underlie this difficulty. First, a single nucleus is usually detected by several low-entropy regions in different focal planes at a single time point. Second, a single nucleus is sometimes detected by several low-entropy regions in the same focal plane at a single time point. Third, it is difficult to determine which focal plane is the top end and which is the bottom end of the focal planes at which a given nucleus is expected to be detected in low-entropy regions, because the appearance of the nucleus becomes gradually blurred as the focal plane becomes farther from the center of the nucleus (Figure 2.1B).

Specificity was defined as the ratio of the number of low-entropy regions detecting nuclei to the number of low-entropy regions produced. Because local image entropy is not sensitive to differences in image quality, particularly in terms of the brightness of the image, I expected that the performance of nuclear detection by examination of low-entropy regions would differ little among sets of 4D DIC microscope images.

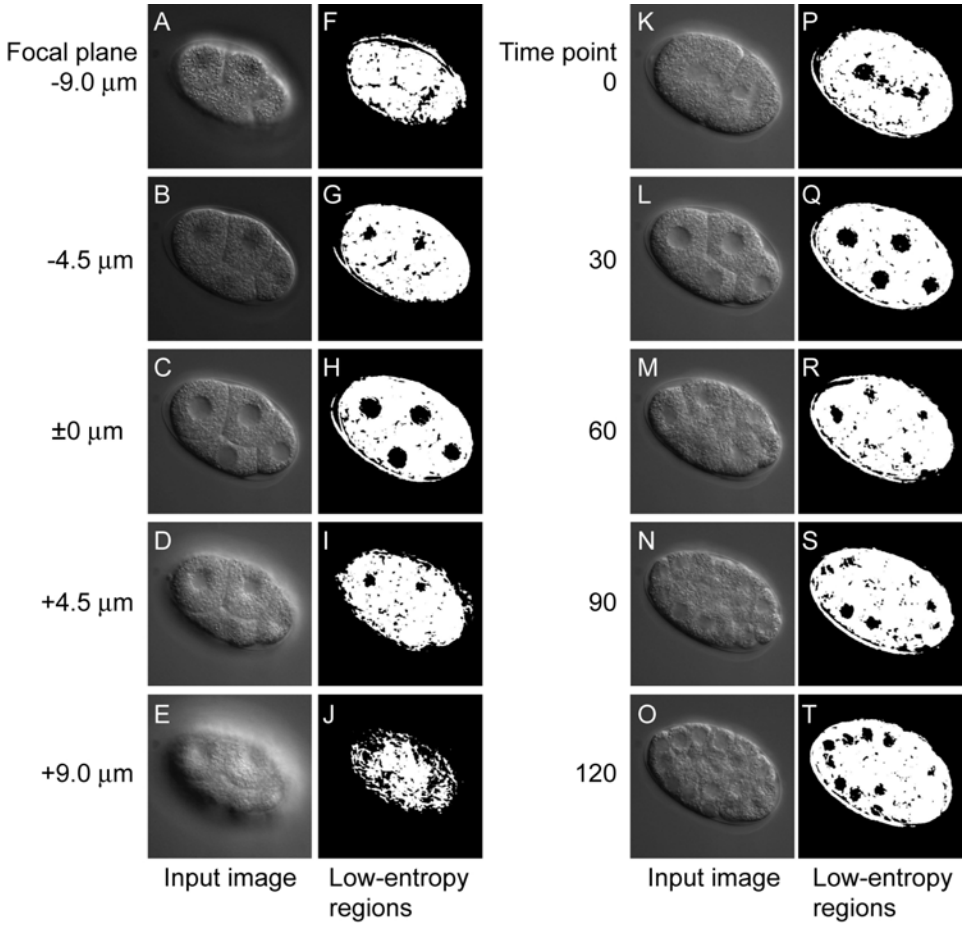

Figure 2.4 Low-entropy regions of different focal planes and different time points. (A–E and K–O) Input images. (F–J and P–T) Low-entropy regions (black) produced from the input images. Low-entropy regions were produced from multifocal images of an embryo at a specific time point in the four-cell stage with 4.5 μm between two focal planes (A–E) and from time-lapse images of an embryo at a specific focal plane with 30 min between two time points (K–L). The low-entropy regions produced are displayed to the right of each input image. The window size was 10 × 10 pixels and the threshold value was 175.

Low-entropy regions that actually detected nuclei were manually selected in five sets of 4D DIC microscope images of an embryo. The resulting five sets of low-entropy regions were used as references to calculate the sensitivity and specificity of nuclear detection. Sensitivity was calculated using low-entropy regions of all time points from time point 0 to that corresponding to the end of the 24-cell stage. Specificity was calculated using low-entropy regions at 11 time points, obtained by sampling every 10 time points from the beginning of the two-cell stage to the end of the 24-cell stage. The number of time points from the beginning of the two-cell stage to the end of the 24-cell stage was 106 on average.

I obtained perfect (= 1.0) sensitivity for all sets of images from the one- to the 24-cell stages (Table 2.2). All nuclei were detected at any time point independently of whether or not they were in the process of cell division. To confirm that this perfect sensitivity was not solely a feature of the five sets of images examined, I produced low-entropy regions from 44 sets of images of *C. elegans* embryos using 10 × 10 pixel windows and threshold values of 175, and then calculated the sensitivity. I obtained perfect sensitivity for all 44 sets of images of embryos from the one- to the 24-cell stages (data not shown). Sensitivity became imperfect in the later stages of embryogenesis, i.e., around the 44-cell stage or later (data not shown). In contrast, very low (< 0.10) specificity was obtained for all sets of images (Table 2.2). In summary, low-entropy regions could be used to detect nuclei in a set of 4D DIC microscope images of *C. elegans* embryos from the one- to 24-cell stages with very high sensitivity and very low specificity. The performance of nuclear detection by low-entropy regions differed little among sets of images.

Table 2.2 Performance of nuclear detection by low-entropy regions and those selected forward and backward trackings

	set 1		set 2		set 3		set 4		set 5	
Low-entropy regions	0.06	(1.0)	0.08	(1.0)	0.06	(1.0)	0.08	(1.0)	0.08	(1.0)
Forward tracking	0.38	(1.0)	0.48	(1.0)	0.55	(1.0)	0.44	(1.0)	0.53	(1.0)
Forward and backward trackings	0.44	(1.0)	0.55	(1.0)	0.67	(1.0)	0.5	(1.0)	0.63	(1.0)

Data are specificity and (sensitivity) for five sets of 4D DIC microscope images of a *C. elegans* embryo from the one- to 24-cell stages (1 set = 56 focal planes × ~120 time points = ~6720 images).

Table 2.3 Number of image sets for which advanced trackings detected nuclei with perfect sensitivity

T_f	T_t					
	1 pixel	4%	8%	12%	16%	20%
1 pixel	5	5	5	4	4	4
30%	5	5	4	4	4	3
50%	5	5	4	4	2	1
70%	5	5	4	4	2	1
90%	1	1	1	1	0	0

Sensitivities of nuclear detection by low-entropy regions selected by advanced forward and backward trackings were calculated for five sets of 4D DIC microscope images of a *C. elegans* embryo from the one- to 24-cell stages. Number of image sets for which sensitivity of nuclear detection were 1.0 is shown.

2.2.6 Selection of low-entropy regions using object-tracking algorithm in the forward direction of time

The very high sensitivity and very low specificity of nuclear detection by using low-entropy regions motivated me to develop a process that selected low-entropy regions that actually detected nuclei. To develop this process, I used spatial and temporal information on the nucleus. In terms of spatial information, I expected the nucleus to be detected by several low-entropy regions, each of which would overlap with another region in an adjacent focal plane at the same time point, because the radius of the nucleus (> 2.5 μm) was much larger than the distance between two adjacent focal planes (0.5 μm). Therefore, a low-entropy region would be more likely to detect a nucleus than others when it overlapped with a region that detected the nucleus in an adjacent focal plane at the same time point. In terms of temporal information, I expected the nucleus to be detected by several low-entropy regions, each of which would overlap with another region in the same focal plane at an adjacent time point, because the nucleus rarely moves more than a distance equal to its diameter (> 5 μm) within the time equal to the interval between two adjacent time points (40 s). Therefore, a low-entropy region would be more likely to detect a nucleus than others when the region overlapped with a region that detected the nucleus in the same focal plane at an adjacent time point.

To select low-entropy regions by using this spatial and temporal information, I used an object-tracking algorithm (Geerts *et al.*, 1987; Lee *et al.*, 1991; Awasthi *et al.*, 1994) (Figure 2.5). The tracking algorithm was composed of the following two recursive processes. First, a low-entropy region in focal plane f at time point t is selected if the region overlaps with a region that has been selected in either focal plane $f - 1$ or $f + 1$ at time point t. Second, a low-entropy region at focal plane f at time point t is selected if the region overlaps with a region that has been selected in focal plane f at time point $t - 1$. Manual selection of a low-entropy region at time point 0 triggers these processes. I call this algorithm *forward tracking* because it tracks nuclei in the forward direction of time.

To examine whether forward tracking effectively selects low-entropy regions that can actually detect nuclei, I applied this algorithm to the low-entropy regions produced from five sets of 4D DIC microscope images of *C. elegans* embryos from the one- to 24-cell stages (Table 2.2). As expected, I obtained perfect sensitivity for nuclear detection by the selected low-entropy regions. All nuclei were detected at any time point, independently of whether or not they were in the process of cell division. Specificity was about 6.7 times better than before selection, although it was still far from perfect. These results indicate that forward tracking effectively selects low-entropy regions that can actually detect nuclei.

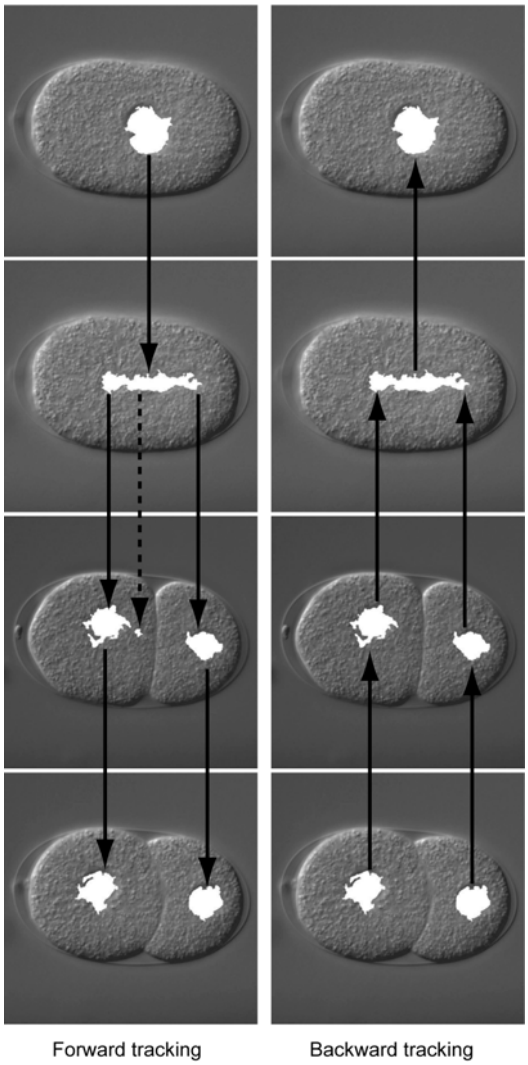

Figure 2.5 Overview of forward and backward trackings. Low-entropy regions selected by forward tracking are shown in the left column and those selected by backward tracking after the selection by forward tracking are shown in the right column. These low-entropy regions (white) are overlaid on their corresponding input images. Solid arrows represent the tracking of low-entropy regions. The broken arrow represents a dead-end branch of tracking.

2.2.7 Further selection of low-entropy regions using object-tracking algorithm in the backward direction of time

To further select low-entropy regions, I used another tracking algorithm. This algorithm, called *backward tracking*, used the same recursive processes as forward tracking, with the exception of the direction of tracking, i.e., it tracked nuclei in the backward direction of time (Figure 2.5). I expected that this backward tracking would be effective for selecting low-entropy regions after forward tracking, because forward tracking usually creates many dead-end branches (Figure 2.5), which

consist of low-entropy regions that do not detect nuclei. Backward tracking selected low-entropy regions that were not included in these dead-end branches (Figure 2.5).

Backward tracking was composed of the following two recursive processes. First, a low-entropy region in focal plane f at time point t is selected if the region overlaps with a region that has been selected in either focal plane $f - 1$ or $f + 1$ at time point t. Second, a low-entropy region in focal plane f at time point t is selected if the region overlaps with a region that has been selected in focal plane f at time point $t + 1$. Manual selection of low-entropy regions at the last time point triggers the processes.

To examine whether backward tracking is effective for selection of low-entropy regions after forward tracking, I applied backward tracking to the five sets of low-entropy regions selected by forward tracking (Table 2.2). Again, I obtained perfect sensitivity for nuclear detection by low-entropy regions selected by backward tracking. All nuclei were detected at any time point independently of whether or not they were in the process of cell division. Sensitivity was markedly better than before backward tracking, although it was still far from perfect. These results indicate that backward tracking is effective for selection of low-entropy regions after forward tracking.

2.2.8 Excellent selection of low-entropy regions using object-tracking algorithm, depending on the extent of overlap between two regions

The very high sensitivity but far lower perfect specificity (0.56 in average) of low-entropy regions selected by the combination of forward and backward trackings motivated me to develop a process that would more effectively select low-entropy regions that could detect nuclei. To develop this process, I used more detailed spatial and temporal information on the nucleus. In terms of more detailed spatial information, I expected the nucleus to be detected by several low-entropy regions, each of which overlapped to a large extent with one of the others in an adjacent focal plane at the same time point, because the 3D shape of the nucleus is usually simple. Therefore, a low-entropy region would become more likely to detect a nucleus when the region overlapped to a large extent with a region that detected the nucleus in an adjacent focal plane at the same time point. In terms of more detailed temporal information, I expected that a nucleus would be detected by several low-entropy regions, each of which overlapped to a certain extent with another in the same focal plane at two adjacent time points, because the nucleus usually moves much less than a distance equal to its diameter within the time equal to the interval between two adjacent time points. Therefore, a low-entropy region would become more likely to detect a nucleus when the region overlapped with a region that detected the nucleus in the same focal plane at two adjacent time points, and when both regions overlapped by a large extent.

To select low-entropy regions using this more detailed spatial and temporal information, I introduced a *minimum overlap ratio* to the forward and backward trackings. The minimum overlap ratio between two low-entropy regions was defined as the smallest ratio of the number of pixels shared by these two regions to the number of pixels making up each region. Thus, when the minimum overlap ratio between two overlapping regions increases, the two regions overlap to a greater extent, i.e., the two regions are more likely to detect the same nucleus. In the forward and backward trackings, I used this minimum overlap ratio to select pairs of low-entropy regions that overlapped to an extent greater than a prefixed value—i.e., pairs of low-entropy regions that were more likely to detect the same nucleus than a prefixed likelihood.

Forward tracking with a minimum overlap ratio was composed of the following two recursive processes. First, a low-entropy region in focal plane f at time point t is selected if the region overlaps with a region that has been selected either at focal plane $f - 1$ or $f + 1$ at time point t by a minimum overlap ratio more than the threshold T_f. Second, a low-entropy region in focal plane f at time point t is selected if the region overlaps with a region that has been selected in focal plane f at time point $t - 1$ by a minimum overlap ratio more than the threshold T_t. Manual selection of a low-entropy region at time point 0 triggers the processes in the same way as with the original forward tracking.

Backward tracking with a minimum overlap ratio is composed of the same recursive processes as forward tracking with a minimum overlap ratio, except that the direction of tracking is reversed—i.e., it tracks nuclei in the backward direction of time in the same way as with the original backward tracking. Manual selection of low-entropy regions at the last time point triggers the processes in the same way as with the original backward tracking. I expected that, as T_f and T_t increased, the selected low-entropy regions would become more likely to detect nuclei.

Table 2.4 Specificity of nuclear detection by low-entropy regions selected by advanced forward and backward trackings

	T_f	T_t					
		1 pixel†	4%	8%	12%	16%	20%
Forward tracking	1 pixel‡	0.48 (0.06)	0.54 (0.11)	0.56 (0.11)	0.56 (0.10)	0.58 (0.10)	0.59 (0.10)
	30%	0.57 (0.08)	0.69 (0.11)	0.74 (0.11)	0.78 (0.10)	0.84 (0.09)	0.87 (0.07)
	50%	0.66 (0.11)	0.79 (0.11)	0.84 (0.08)	0.87 (0.07)	0.90 (0.06)	0.94 (0.03)
	70%	0.74 (0.12)	0.86 (0.08)	0.90 (0.07)	0.93 (0.05)	0.94 (0.05)	0.97 (0.03)
	90%	0.83 (0.10)	0.93 (0.04)	0.95 (0.03)	0.98* (0.01*)	0.99* (0.01*)	1.00* (0.00*)
Forward and backward trackings	1 pixel‡	0.56 (0.08)	0.62 (0.13)	0.64 (0.13)	0.65 (0.12)	0.67 (0.13)	0.69 (0.13)
	30%	0.70 (0.10)	0.83 (0.12)	0.87 (0.09)	0.90 (0.07)	0.93 (0.05)	0.95 (0.03)
	50%	0.82 (0.12)	0.91 (0.07)	0.93 (0.05)	0.95 (0.05)	0.97 (0.04)	0.98 (0.02)
	70%	0.87 (0.11)	0.96 (0.05)	0.97 (0.04)	0.99 (0.02)	0.99 (0.01)	1.00 (0.00)
	90%	0.93 (0.08)	0.99 (0.01)	1.00 (0.00)	1.00* (0.00*)	1.00* (0.00*)	1.00* (0.00*)

Data are mean and (SD) for five sets of 4D DIC microscope images of a *C. elegans* embryo from the one- to 24-cell stages. *Data are for four sets of DIC microscope images, because no low-entropy regions were selected in one image set. †Low-entropy regions were selected when they shared at least one pixel with regions already selected in the same focal plane at an adjacent time point, i.e., the same condition as used for the original forward and backward trackings. ‡Low-entropy regions were selected when they shared at least one pixel with regions already selected in an adjacent focal plane at the same time point, i.e., the same condition as used for the original forward and backward trackings.

To examine whether the combination of forward and backward trackings with minimum overlap ratio (hereafter called *advanced forward and backward trackings*) would more effectively select low entropy regions than a combination of the original forward and backward trackings, I applied this combination of advanced forward and backward trackings to the low-entropy regions produced from five sets of 4D DIC microscope images of *C .elegans* embryos from the one- to 24-cell stages. Various sets of T_f and T_t were examined (Table 2.3 and Table 2.4). As expected, as T_f and T_t increased, the specificity of detection by the selected low-entropy region increased, whereas the sensitivity of detection by the region decreased. I found many sets of T_f and T_t that provided very high specificity (= 1.0), and several of them also provided perfect sensitivity (for example, T_f = 70% and T_t = 4% in Table 2.4). In this set of T_f and T_t, the selected low-entropy regions nearly perfectly detected all nuclei at any time point, independently of whether or not the nuclei were in the process of cell division. These results indicate that the combination of advanced forward and backward trackings more effectively selected low-entropy regions than did the combination of original forward and backward trackings. When an optimal set of T_f and T_t was applied, the combination of advanced forward and backward trackings nearly perfectly selected low-entropy regions that could detect nuclei.

2.3 Discussion

2.3.1 Less sensitivity of this system to differences in image quality than that of Yasuda *et al.*'s system

This system is less sensitive than Yasuda *et al.*'s system to differences in image quality (Yasuda *et al.*, 1999). The difference in local image entropy (the image texture measure used in the new system) between nucleus and cytoplasm is remarkably greater than that in the image texture measure used in Yasuda *et al.*'s system (hereafter called *Yasuda et al.'s measure*) (Figure 2.3). The difference in local image entropy at the boundary between nucleus and cytoplasm is remarkably greater than that in Yasuda *et al*.'s measure.

Yasuda *et al.*'s system (Yasuda *et al.*, 1999) used edge-detection operators, that is, Kirsch and the Prewitt operators, to detect nuclei from DIC microscope images. Because these edge-detection operators are very sensitive to differences in the intensity of local pixels, the output values of these operators varied widely in both the nucleus and cytoplasm. Therefore, application of thresholding directly to the images resulting from image conversion using these operators did not effectively discriminate between nucleus and cytoplasm.

To deal with this problem, Yasuda *et al.*'s system applied a blur filter to the images resulted from image conversion. The combination of the edge-detection operator and the blue filter was the Yasuda *et al.*'s measure. The blur filter reduced the variation of the output values of the edge-detection operators, so that the thresholding of the resulting images allowed discriminating the image textures of the nucleus and the cytoplasm. However, the gradient at the boundary between nucleus and cytoplasm becomes easier than that of local image entropy (Figure 2.3). Thus, the nuclear detection using Yasuda *et al.*'s measure was more sensitive to the differences in image quality, so that size of nuclear region with Yasuda *et al.*'s measure would change greater than that of my system when the threshold values are changed by the same value. Yasuda *et al.*'s system therefore required laborious hand-tuning of the thresholding each time a new image set was applied.

2.3.2 Advantage of this system

One major advantage of this system is the use of local image entropy to quantify the appearance of the nucleus in the images. Yasuda *et al.*'s system used edge detection operators to quantify the appearance of the nucleus (Yasuda *et al.*, 1999). Because these operators were sensitive to differences in image quality (e.g., brightness, contrast) among sets of images, Yasuda *et al.*'s system required laborious hand-tuning of system parameters each time a new image set was used (section 2.2.4 and section 2.3.1). Local image entropy is not sensitive to differences in image quality among sets of images because it represents the smoothness of the image texture (section 2.2.1). Therefore, my system can be applied to different image sets without the need to change the system parameters. I applied five sets of 4D DIC microscope images to my system, and the system detected the nuclei in these sets with similar sensitivity and specificity when I used the same parameter values (Table 2.2). This reduced sensitivity to differences in image quality makes my system applicable to research. I can apply this system to sets of 4D DIC microscope images of mutant *C. elegans* embryos (Figure 2.6) and embryos in which specific genes are silenced by RNA interference (Figure 2.7).

Another major advantage of my system is the use of object-tracking algorithms to examine all regions with the features of the image texture of the nucleus (i.e., low local image entropy) in a set of 4D DIC microscope images and to select regions that can actually detect nuclei. A DIC microscope image of a *C. elegans* embryo contains many regions that have similar (smooth) image textures to that of the nucleus but that do not actually correspond to the nucleus, such as the boundaries between cells and the spaces between the embryo and the eggshell (Figure 2.4). Thus, in addition to image texture, other features of the nucleus are needed to completely distinguish the nucleus. Yasuda *et al.*'s system used the (round) shape of the nucleus that was not in the process of cell division in addition to the feature of image texture, as quantified by edge detection operators (Yasuda *et al.*, 1999). Yasuda *et al.*'s system could not detect nuclei in the process of cell division. The object-

tracking algorithm in my system uses spatial and temporal information on the nucleus, and this information is independent of the process of cell division. Thus, my system detects all nuclei—whether or not the cell is dividing—at every time point from one- to 24-cell stages. This continuous detection of nuclei is a great help in following the CDP.

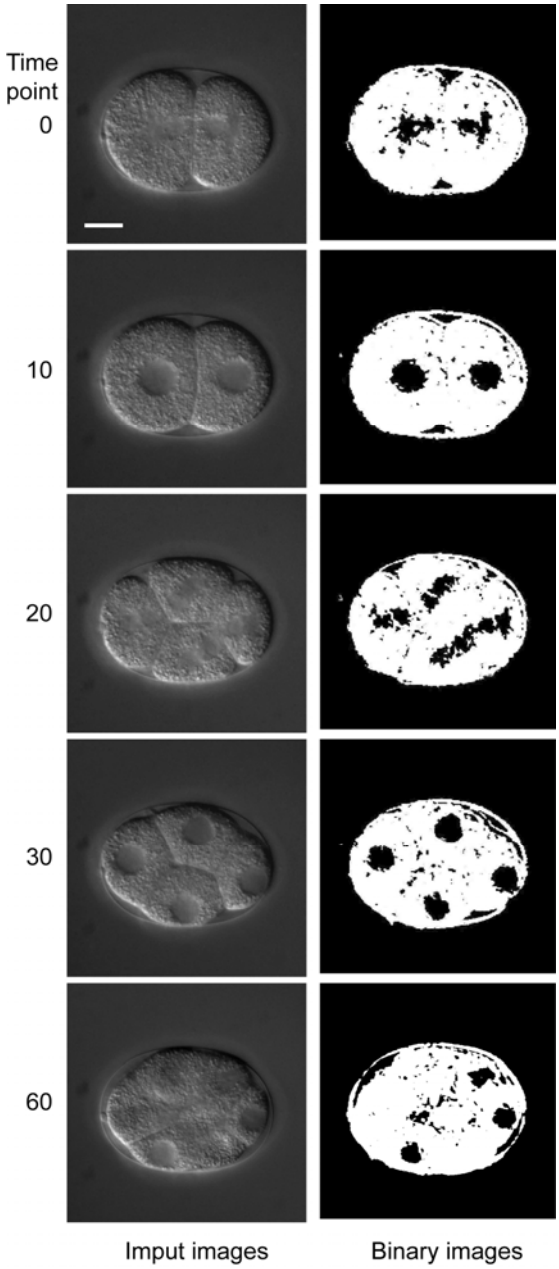

Figure 2.6 Low-entropy regions in a *par-1* embryo. Input images of a *par-1* embryo are shown in the left column and low-entropy regions (black) are shown in the right column. Bar is 10 μm.

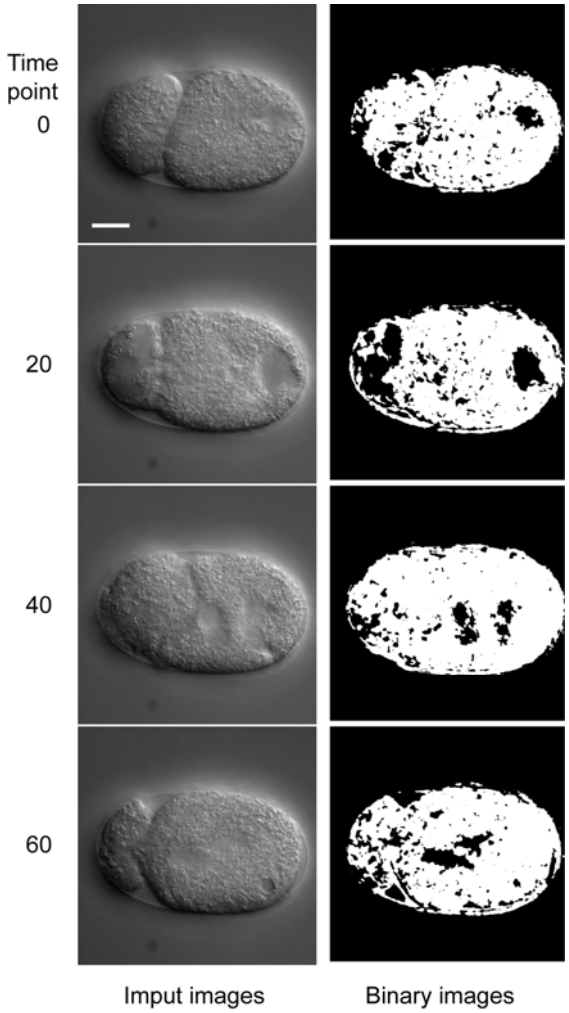

Figure 2.7 Low-entropy regions in a *tba-2(RNAi)* embryo. Input images are shown in the left column and low-entropy regions (black) are shown in the right column. Bar is 10 μm.

My system effectively detected nuclei over a markedly longer developmental period than Yasuda *et al.*'s system did, i.e., from the one- to 24-cell (Table 2.3 and Table 2.4) stages compared with only the two- to eight-cell stages (Yasuda *et al.*, 1999). This extension of the period of effective nuclear detection primarily results from the very high sensitivity of nuclear detection by low-entropy regions before forward and backward trackings (Table 2.2). The sensitivity and specificity of nuclear detection by these "original" low-entropy regions depend on the parameters used to produce the regions (i.e., window size and entropy threshold): the higher the sensitivity, the lower the specificity. My system uses a set of values for these parameters that provides very high sensitivity and very low specificity of nuclear detection by the original low-entropy regions (Table 2.2), because subsequent forward and backward trackings effectively distinguish those regions that actually detect nuclei from those that do not.

Yasuda *et al.*'s system used a two-step strategy similar to my system: i.e., regions that had the image texture of the nucleus were produced using edge detection operators, and from these "likely nuclear" regions, those that actually detected nuclei were selected using the shape of the nucleus. The sensitivity and specificity of nuclear detection by these "original" likely nuclear regions depended on the parameters used to produce the regions. However, the shape-dependent selection of likely nuclear regions was far less effective than the selection of low-entropy regions by forward and backward trackings. Thus, Yasuda *et al.*'s system used a set of parameter values that provided markedly lower sensitivity and markedly higher specificity of nuclear detection by the original likely nuclear regions than by the original low-entropy regions. In the current study, I found very high sensitivity of nuclear detection by the original low-entropy regions up to the 44-cell stage (data not shown). Thus, improvement in the selection of low-entropy regions will further extend the period of effective nuclear detection. I am developing an improved system that uses both a tracking algorithm and the known shape and size of nuclei in non-dividing cells to select low-entropy regions.

Fluorescent labeling of nuclei is a method that has recently been developed for identifying the positions of the nuclei in living *C. elegans* embryos (Kelly *et al.*, 1997; Praitis *et al.*, 2001). With this method, the genetic information of an embryo is artificially modified so that the embryo expresses nuclear protein fused with fluorescent protein, such as histone H2B fused with green fluorescent protein (GFP) (Praitis *et al.*, 2001); the embryo is illuminated by excitatory light (e.g., blue or UV light for GFP), and the expressed fusion protein produces light of a specific color (e.g., green for GFP). Because the nuclei are labeled with a specific color, detection of the nuclei is much easier than that using the DIC microscope. However, the development of the embryo expressing the fusion protein may differ from that of the intact embryo because of the presence of GFP or the modification of genetic information (Fire, 1986; Liu *et al.*, 1999; Zhang *et al.*, 2002). Fluorescent labeling can be used to visualize nuclei for a markedly shorter period than with the DIC microscope because of photobleaching: i.e., the intensity of fluorescence of the fusion protein decreases because of exposure of the protein to the excitatory light (Strome *et al.*, 2001), although the amount of photobleaching can be reduced by the use of multiphoton fluorescence imaging (Denk *et al.*, 1990). In contrast, the DIC microscope can be used to visualize the nuclei of an intact embryo throughout the development of *C. elegans*. Therefore, to describe the precise position of nuclei in living *C. elegans* embryos, identification of the position of the nucleus using the DIC microscope seems more suitable than that using fluorescent labeling of nuclei.

2.3.3 Drawback of this system

A major drawback of my system is the need for manual selection of low-entropy regions at the first and last time points. These manual operations may reduce the objectivity and productivity of my system, because selection is determined by the operator. However, slight differences in manual selection at the first and the last time points does not influence the automated selection of low-entropy regions in between these points, because the automated selections select all regions that overlap with other selected regions in the adjacent focal plane at the same time point or in the same focal plane at the adjacent time point. Thus, usually my system objectively detects nuclei in between the first and last time points. Manual selection of low-entropy regions at the first and the last time points could still reduce the productivity of my system, because these manual selections usually take about 10 min. However, my system still markedly increases the productivity of identification of the positions of the nuclei in *C. elegans* embryos, because manual selection of low-entropy regions for all time points from the one- to 24-cell stages (56 focal planes × ~120 time points = ~6720 images) takes more than 50 h. My system needs about 135 min for computation (120 min for the production of low-entropy regions and 15 min for the forward and backward trackings) and 10 min for manual operations to detect all the nuclei in a set of 4D DIC microscope images of a *C. elegans* embryo recorded from the one- to 24-cell stages. These times for computation and manual operations are acceptable in research. The selection of low-entropy regions at the first and last time points will be automated, most likely by using known properties of nuclei, such as the known shapes and sizes of nuclei in non-dividing cells.

2.3.4 Limitation of nuclear detection

The low-entropy regions before selection by the forward and backward trackings failed to detect nuclei at around the 44-cell stage or later. Because the window size (10 × 10 pixels) and the threshold value (175) used in this experiment appear likely to be optimal for my system, the result indicates that the limit of my system is around the 44-cell stage. I believe that this limit comes from the reduction in size of the cells during embryogenesis. As the size of the cells decreases during embryogenesis, the distance between the nucleus and cell membrane decreases. Usually at around the 44-cell stage, some nuclei are positioned so close to the cortex of the embryo that a 10 × 10 pixel window cannot produce a high-entropy (> 175) boundary between the nucleus and the image background; the texture of the image background is smooth (Figure 2.2), and thus the local image entropy in the image background is as low as that in the nucleus. In this situation, the low-entropy regions corresponding to the cortically positioned nucleus merge with the low-entropy regions corresponding to the image background. Because my system removes the low-entropy regions corresponding to the image background, the low-entropy regions produced by my system fail to detect the cortically positioned nucleus. To overcome this limitation, modulation of the window size

and/or the threshold value depending on the embryonic stage and/or position of the nucleus within the embryo (central or cortical) might be effective. I observed that low-entropy regions produced using a smaller (< 10 × 10 pixel) window size and/or smaller (< 175) threshold value successfully discriminated between such cortically positioned nuclei and the image background in the later stages of embryogenesis.

2.3.5 Applicability

This system is applicable to research programs that require high objectivity and/or productivity of identification of the positions of the nuclei in *C. elegans* embryos. Because the sensitivity and specificity of nuclear detection in this system depend on the thresholds for minimum overlap ratios (T_f and T_t), the values of these thresholds should be specified when the system is applied to a specific study. I often use T_f = 70% and T_t = 4%, because sensitivity is often more important than specificity in research programs. I applied this system to an automated CDP measurement system for *C. elegans* embryos (Hamahashi *et al.*, 2006) (explained in Chapter 3). In addition, this system has been used to measure the positions of the male pronucleus (the sperm-derived nucleus) in a very early *C. elegans* embryo; the measurements were compared with computer simulations to determine the mechanism that specifies the positions of the male pronucleus during the very early period of *C. elegans* development (Kimura and Onami, 2005).

2.4 Summary

In this chapter, I presented a system that I have developed to automate the detection of nuclei in a set of 4D DIC microscope images of *C. elegans* embryo. This system can be applied to multiple image sets without the need to change parameter values. This system can detect nuclei that are in and not in the process of cell division from fertilization to the onset of gastrulation, i.e., from the one- to 24-cell stages.

Methods

Preparation of 4D DIC microscope images of *C. elegans* embryos

The Bristol N2 *C. elegans* was cultured under standard conditions (Brenner, 1974). An embryo immediately after fertilization (before meeting of the female and male pronuclei) was dissected from a hermaphrodite and mounted on a 2% agar pad on a glass slide, covered with a coverslip, and sealed with petroleum jelly. Nomarski DIC microscope images were obtained using a Leica DMRE microscope equipped with an HCX PL APO 100×/1.40 NA objective, whose illumination intensity and objective-side Wollaston prism were adjusted to obtain images of the same quality. Digital

images of 600 × 600 pixels with 256 gray levels (0.1 μm per pixel) were recorded with an ORCA CCD Camera (Hamamatsu Photonics), and the recording system was controlled by IP Lab 3.5 software (Scanalytics). Digital images of the developing embryo were recorded at 22°C in 56 focal planes, with a distance of 0.5 μm between two focal planes, and a set of 56 focal plane images was recorded every 40 s for 2 h.

Hardware and software environment

Because I needed to process many images, low-entropy regions were produced from sets of 4D DIC microscope images using a Beowulf-class PC cluster (Sterling *et al.*, 1995) consisting of 48 nodes, each of which used a 2 GHz Intel Pentium 4 processor, 1 GB of SDRAM memory, and a 100 Base-TX Ethernet card. Parallel Virtual Machine software (Sunderam, 1990) was used for communications between the nodes. In my implementation, each image in a set of 4D DIC microscope images was sent to a node that used a single CPU. The forward and backward trackings for selection of low-entropy regions were processed on a single processor PC that used a 2.2 GHz Intel Pentium 4 processor and 1 GB of RDRAM memory. The programs were written in C and C++.

Chapter 3 Main system: a system measuring the pattern of cell divisions

3.1 Introduction

Yasuda *et al.* attempted to develop a system that would measure a CDP in a *C. elegans* embryo (Yasuda *et al.*, 1999). Their system first detects nuclei by producing image regions that are candidates of nuclear regions and by selecting nuclear regions from candidates. Then, their system identifies a CDP by tracking nuclear region along a time line from 2- to 8-cell stages. Though their system identifies a CDP, their system can not measure a timing of cell division. Because their system selects nuclear regions based on the roundness of the shape of nuclear region, their system can not select nuclear regions whose shapes are not round. Because the shapes of nuclei that are in the process of cell division usually are not rounded shaped, their system can not detect such nuclei. Therefore, their system can not measure the timing at which the cell division occurs. In addition, the maximum cell stage of their tracking is limited under eight-cell stage. Because their system can not detect the nuclei that are in the process of cell division, their system can not continue to track nuclear regions when nuclei start dividing. To continue to track nuclear regions, their system infers the most likely region detecting a daughter nucleus to be tracked from a nuclear region detecting a mother nucleus, based on the nearest-neighbor rule of 3D distance and time between nuclear regions. Because of their inference basis, their system is hard to infer a proper nuclear region to be tracked, if many cells (after the 8-cell stage) divide almost at the same time and/or the distances between cells become short.

To measure a CDP of a *C. elegans* embryo, I first developed a system (Hamahashi *et al.*, 2005) that detects nuclei in a set of 4D DIC microscope images of *C. elegans* embryo from one- to 24-cell stages (hereafter this system is called a *nuclear detection system (NDS)*) (presented in Chapter 2). NDS detects nuclei with low-entropy regions (section 2.2.1) that are candidates of nuclear regions produced by binarizing the local image entropy (Handmann *et al.*, 2000). Among low-entropy regions, nuclear regions and the other image regions (i.e. boundaries between cells and spaces between the embryo and the eggshell; hereafter these regions are called *non-nuclear regions*) are involved. NDS, differently from Yasuda *et al.*'s system, does not use the shapes of nuclear regions to select nuclear regions from low-entropy regions, but uses the forward and backward trackings (section 2.2.6, section 2.2.7 and section 2.2.8). These trackings allow selecting nuclear regions that

detect nuclei that are in and not in the process of cell division. Then, I developed a system that measures a CDP of a *C. elegans* embryo (Hamahashi *et al.*, 2006).

In this chapter, I present a system that measures a CDP in *C. elegans* embryo from one- to 24-cell stages (Hamahashi *et al.*, 2006). This system objectively and productively detects nuclei using nuclear regions produced by NDS (Chapter 2). This system first produces nuclear regions from a set of 4D DIC microscope images using the basic system. Then, this system identifies the 3-dimensional (3D) region of each nucleus by a unit that groups nuclear regions detecting the same nucleus (explained in section 3.2.3). Finally, this system tracks units along a time line and outputs a tracking trajectory that is the measured CDP. If a unit groups inappropriate nuclear regions, this system detects the group and corrects it (such as cuts and/or merges nuclear regions) to make a new group of modified nuclear regions (explained in section 3.2.4). If this system inappropriately tracks units (nuclei detected by a tracker and a tracked units are different), this system detects this failure and corrects it (explained in section 3.2.4). GUIs have been implemented in this system to enable manually assisting automated tasks in case those tasks fail. This system allows almost automatically measuring a CDP in a *C. elegans* embryo from one- to 24-cell stages, where the objectivity and productivity of the measurement are high.

3.2 Results

3.2.1 Overview of the main system measuring CDP

The system, which I have developed (Hamahashi *et al.*, 2006) to measure CDP of *C. elegans* embryos, consists of a 4D DIC microscope system, image analysis software, statistical analysis software, and visualization software (Figure 3.1A). The 4D DIC microscope system records a set of multifocal time-lapse images of a *C. elegans* embryo. The image analysis software measures a CDP from a set of 4D DIC microscope images. The image analysis software consists of three modules designed for nuclear detection, nuclear lineaging, and error-correction. The statistical analysis software analyses CDPs among wild-type and mutant embryos using the statistical package R (R-project). The visualization software visualizes a CDP in a computer display and 3-dimensionally rotates the CDP to view from any angle (Figure 3.1B).

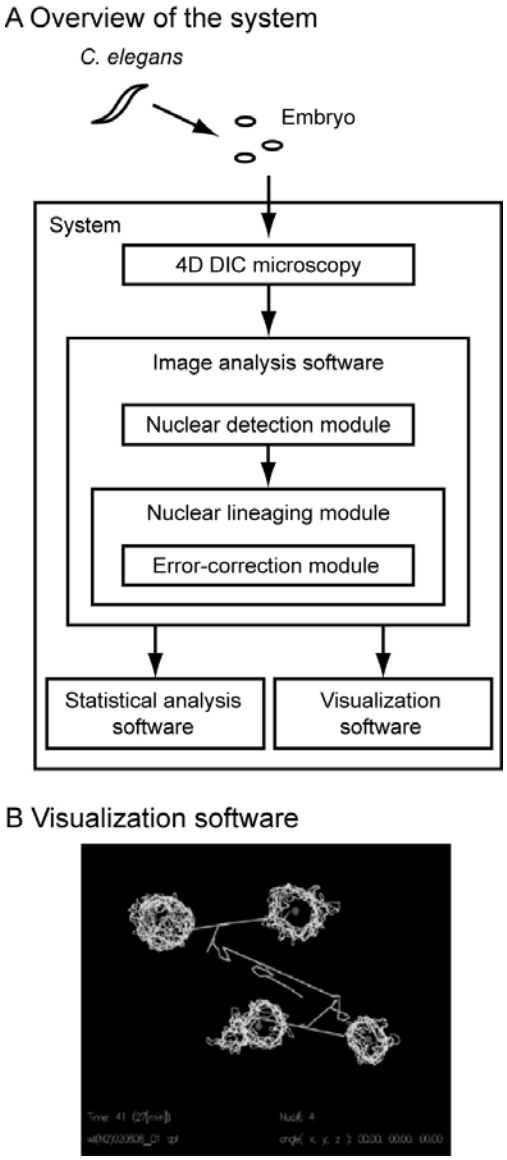

Figure 3.1 Overview of the system and the visualization software.

3.2.2 Nuclear detection module

The nuclear detection module (NDM) detects nuclei in a set of 4D DIC microscope images of *C. elegans* embryo (Figure 2.1B) using NDS (Hamahashi *et al.*, 2005) (Chapter 2). NDM is mostly the same as NDS, but has a GUI (Figure 3.2). To detect nuclei, NDM produces low-entropy regions (Figure 3.3) that are candidates of nuclear regions. These candidates consist of nuclear regions and non-nuclear regions. NDM selects nuclear regions from candidates using the forward and backward trackings (Hamahashi *et al.*, 2005) (section 2.2.6, section 2.2.7 and section 2.2.8). GUI has been implemented to allow manually selecting nuclear regions in case nuclear regions are not selected by forward and backward trackings, or allow manually removing remaining non-nuclear regions in case non-nuclear regions are selected by the trackings.

Figure 3.2 Snapshot of graphical user interface in the nuclear detection module.

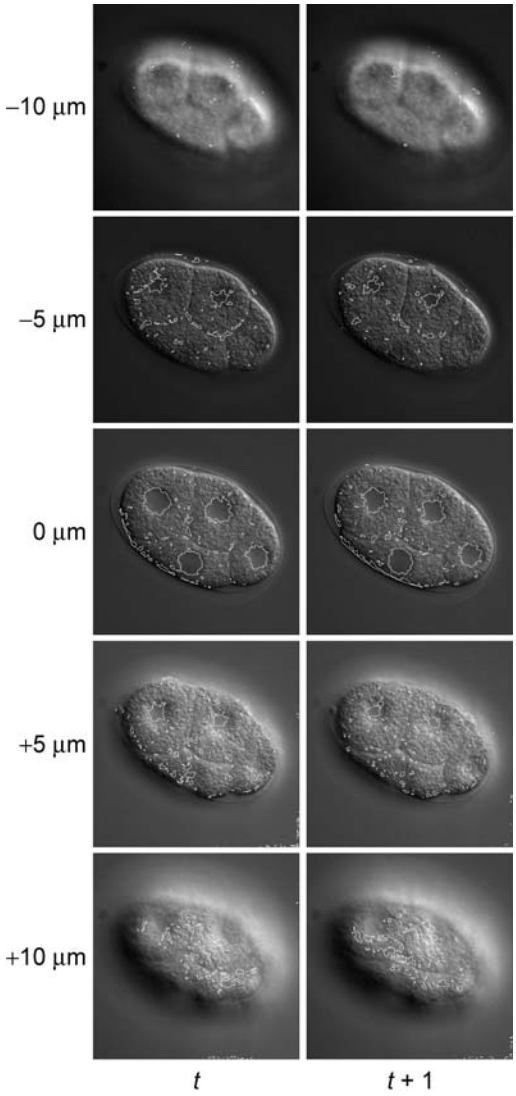

Figure 3.3 Low-entropy regions produced by local image entropy. The white lines enclose low-entropy regions.

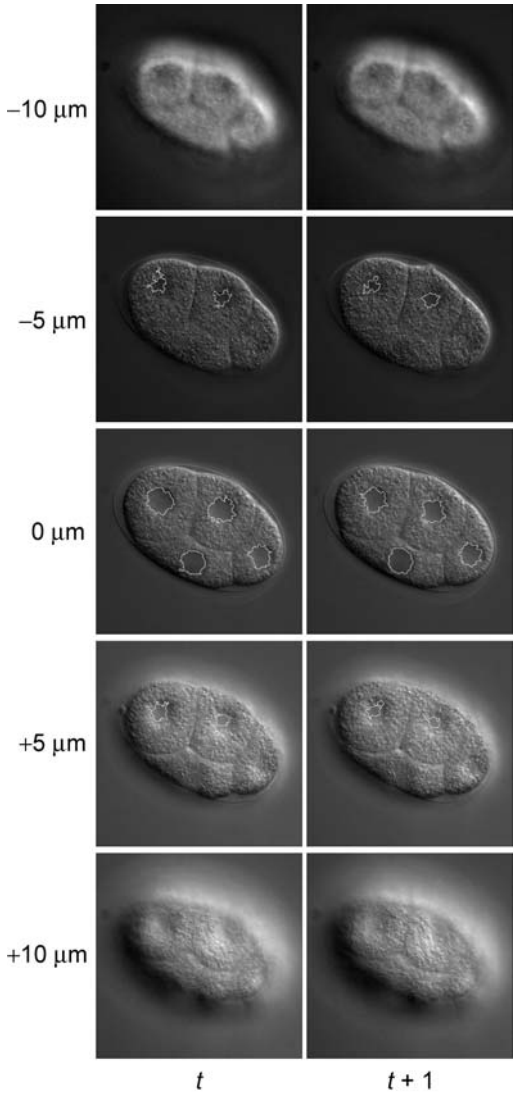

Figure 3.4 Nuclear regions after the removal of non-nuclear regions. The white lines enclose nuclear regions.

3.2.3 Nuclear lineaging module

The nuclear lineaging module (NLM) measures a CDP using nuclear regions through two steps (detailed procedures of these steps are explained in this section). In the step 1, NLM identifies a 3D region of each nucleus. Each 3D region is called a *unit* that groups nuclear regions that detect the same nucleus at each time point. In the step 2, NLM tracks units along a time line to obtain the tracking trajectory. This tracking trajectory is the measured CDP. NLM involves the error-correction module (ECM) (explained in section 3.2.4) which automatically corrects errors occurred in the step 1 and 2.

The concept of unit has been specially designed to identify a 3D region of each nucleus, because there are complications in this identification using nuclear regions. Usually, several nuclear regions detect the same nucleus at a single time point, because the diameter (> 5 μm) is larger than the distance between adjacent focal planes (0.5 μm) and NDM produces nuclear regions in focal planes for each nucleus. Furthermore, even in a single focal plane, NDM sometimes separately produces nuclear regions that detect the same nucleus (Figure 3.5). Among these nuclear regions, NLM had to identify nuclear regions that detected the same nucleus. Because each unit groups nuclear regions that detect the same nucleus, it can represent a 3D region of each nucleus. Once units are produced, CDP is expected to be measured as a tracking trajectory obtained by tracking units along a time line from one-cell stage.

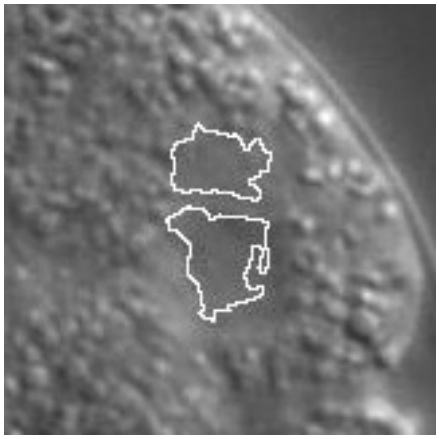

Figure 3.5 Nuclear regions separately produced by the nuclear detection module. The white lines enclose nuclear regions. The nuclear detection module separately produced nuclear regions that detected the same nucleus.

Step 1: This step identifies 3D regions of each nucleus using nuclear regions. The nuclear regions 2-dimensionally detect nuclei in a set of 4D DIC microscope images. To identify 3D regions of nucleus, I used spatial information on the nucleus, similarly to the forward tracking algorithm

(section 2.2.6). I expected that the nucleus should be detected by several nuclear regions each of which would overlap with a region detecting the same nucleus in an adjacent focal plane at the same time point, because the radius of the nucleus (> 2.5 μm) was larger than the distance between two adjacent focal planes (0.5 μm). Therefore, nuclear regions detecting the same nucleus are expected to be produced at almost the same XY-position in focal planes. Thus, this step checked every combination of nuclear regions over all focal planes at each time point to find out which nuclear regions overlapped when they were projected onto the XY-plane (Figure 3.6A). This step groups overlapping regions; each group is called a unit (hereafter each nucleus is considered to be "detected" by each unit).

Step 2: This step tracks units along a time line to obtain a tracking trajectory. To track units, I used temporal information on the nucleus, similarly to the forward tracking algorithm (section 2.2.6). I expected that the nucleus should be detected by several nuclear regions each of which would overlap with a nuclear region detecting the same nucleus in the same focal plane at an adjacent time point, because the nucleus rarely moves more than a distance equal to its diameter (> 5 μm) within the interval between two adjacent time points (40 s). Therefore, a nuclear region would be more likely to detect a nucleus than others when the nuclear region overlapped with a nuclear region that detected the nucleus in the same focal plane at an adjacent time point. Thus, this step checked every combination of nuclear regions, one of which was grouped in a unit U_t at a time point t and the other of which was grouped in a unit U_{t+1} at the time point $t + 1$, in each focal plane to find out which nuclear regions overlapped when they were projected onto the XY-plane. If nuclear regions overlap, U_t and U_{t+1} were considered to detect the same nucleus (hereafter this situation is referred to as "U_t tracks U_{t+1}"; U_t and U_{t+1} are called a *tracker unit* and a *tracked unit*, respectively).

After processing the step 1 and 2, NLM outputs a tracking trajectory of units as the measured CDP. In the tracking trajectory, NLM describes the time point, the tracker unit's ID, the tracked unit's ID, and the 3D position of the tracked unit. In NLM, GUI has been implemented to enable us to manually trigger the tracking of units from any unit; the front end of this GUI is the same as that implemented in NDM (Figure 3.2). This GUI also enables the step 2 to continue tracking units when the step 2 fails to track units automatically. This failure is occurred when no nuclear regions in the same focal plane are produced in both U_t and U_{t+1}, even if U_t and U_{t+1} detect the same nucleus, or when the nucleus moves more than a distance equal to its diameter within one time interval.

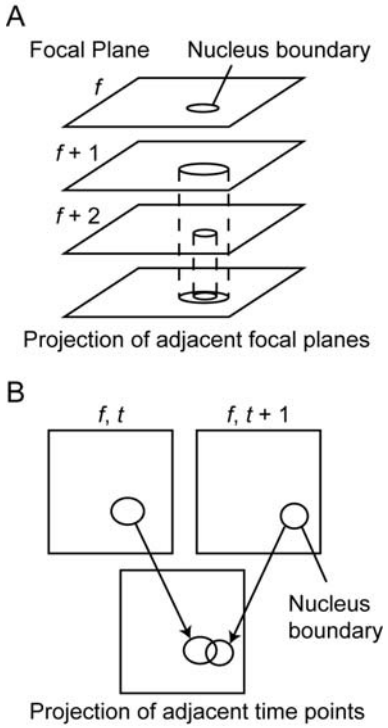

Figure 3.6 Step 1 and step 2 in the nuclear lineaging module. (A) Step 1: NLM produces units by checking whether nuclear regions in adjacent focal planes overlap or not. (B) Step 2: NLM tracks units by checking whether nuclear regions in the same focal plane at adjacent time points overlap or not.

3.2.4 Error-correction module

The error-correction module (ECM) automatically corrects making of units (in the step 1) and tracking of units (in the step 2) by referring a resulted tracking trajectory. Because of the design concept of unit to obtain a tracking trajectory as a CDP, as described in section 3.2.3, each nucleus has to be detected by only one unit, and each unit has to detect only one nucleus. In addition, because the CDP is expected to be obtained by tracking units along a tine line from one-cell stage, the units have to be tracked properly; in other words, a tracker unit and its tracked unit have to detect the same nucleus. However, following three types of errors occurred in step 1 and 2; (1) a nucleus is sometimes detected by more than one unit, (2) a unit sometimes detects more than one nucleus, and (3) a tracker unit and its tracked unit detect different nuclei. The error (1) occurs because nuclear regions that detect the same nucleus are separately produced by NDM (Figure 3.5) and units that detect the same nucleus will be separately made. The error (2) occurs because falsely merged nuclear regions each of which detects more than two nuclei are produced by NDM (Figure 3.7) and units each of which detects more than two nuclei are made. The error (3) occurs because nuclei are positioned closely and some nuclear regions that detect different nuclei, falsely overlap. To measure CDP, therefore, ECM that automatically corrects those errors was needed. Especially for the error

(3), it was conditioned that the tracker unit always tracks both two units, one of which detects a different nucleus from that detected by the tracker unit, and the other of which detects the same nucleus as that detected by the tracker unit. (This condition is empirically natural because all CDPs ($N = 23$) satisfied this condition.)

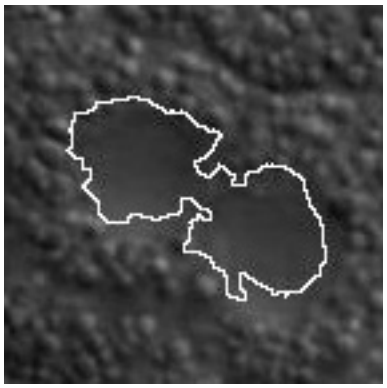

Figure 3.7 Falsely merged nuclear region produced by the nuclear detection module. The white line encloses a nuclear region. The nuclear detection module falsely merged nuclear regions that should be separately produced.

3.2.4.1 Protocol of error correction

First, ECM detects an error without discriminating errors (1), (2) and (3). Let U_t^A be a unit detecting a nucleus A at a time point t. If any error does not present in a tracking trajectory, U_t^A should track a single unit U_{t+1}^A when the detected nucleus is not in the process of cell division, or U_t^A should track two units, $U_{t+1}^{a'}$ and $U_{t+1}^{a''}$, when the detected nucleus is in the process of cell division where a' and a'' are A's daughter nuclei. (That is to say, one unit always tracks one or two units if no errors present in a tracking trajectory.) Consider the case that the error (1) presents in a tracking trajectory, in which a nucleus x at a time point t is detected by more than one unit; hereafter two units such as $U_t^{x'}$ and $U_t^{x''}$ are used for the simplification of explanation. $U_t^{x'}$ and $U_t^{x''}$ should track the same unit U_{t+1}^x (Figure 3.8A). (If $U_t^{x'}$ and $U_t^{x''}$ track $U_{t+1}^{x'}$ and $U_{t+1}^{x'}$ respectively, their tracked units $U_{t+k}^{x'}$ and $U_{t+k}^{x''}$ always track the same unit within a few time points. In other words, except for the set of 4D DIC microscope images whose recording is finished at a time point just after a nucleus is detected by more than one unit, the units detecting the same nucleus always track the same unit within a few time points.) Consider the case that the error (2) presents in a tracking trajectory, in which nuclei x and y at a time point t are detected by a single unit $U_t^{x,y}$. In this case, U_{t-1}^x and U_{t-1}^y, which detect x and y respectively at a time point $t - 1$, should track $U_t^{x,y}$. Consider the case that the error (3)

presents in a tracking trajectory, in which U_t^x detecting a nucleus x at a time point t tracks U_{t+1}^y detecting a nucleus y at a time point $t + 1$. In this case, because of the condition of error (3) described in the previous paragraph, U_{t+1}^y should be tracked by not only U_t^x but also U_t^y detecting a nucleus y at a time point t (Figure 3.8C). Consequently, viewing errors (1), (2) and (3) together, any of errors (1), (2) and (3) can be detected, if a case that more than one unit in a time point τ track the same unit in a time point $\tau + 1$ is detected. (In this dissertation, a unit tracked by more than one unit is called "merged unit", because this unit merges the more than one pathway in a tracking trajectory.)

Next, ECM discriminates the detected error as the error (1), (2) and (3). Usually, several merged units are presented in a tracking trajectory. ECM focuses on a merged unit U_{t_0} that presents at the earliest time point among all merged units. Then, ECM detects *singular units* among all units. The singular unit is defined as the unit which detects only one nucleus and whose detected nucleus is detected by only this unit (the method to detect the singular units is explained in section 3.2.4.2). After the detection of singular units, ECM checks whether $U_{t_0-1}^{'}$ and $U_{t_0-1}^{''}$, both of which track U_{t_0}, detect the same nucleus or not. When either or both of $U_{t_0-1}^{'}$ and $U_{t_0-1}^{''}$ are singular units, ECM determines that $U_{t_0-1}^{'}$ and $U_{t_0-1}^{''}$ detect different nuclei. When both $U_{t_0-1}^{'}$ and $U_{t_0-1}^{''}$ are not singular units, ECM finds singular units at a time point $t_0 - 2$ to complete this check. Because of the definition of U_{t_0}, any merged unit does not present at earlier time points than t_0, so that only two cases present when $U_{t_0-1}^{'}$ and $U_{t_0-1}^{''}$ are tracked by units at $t - 2$. One case is that $U_{t_0-1}^{'}$ and $U_{t_0-1}^{''}$ are tracked by $U_{t_0-2}^{'}$ and $U_{t_0-2}^{''}$ respectively, and the other case is that $U_{t_0-1}^{'}$ and $U_{t_0-1}^{''}$ are tracked by the same unit U_{t_0-2}. ECM determines that $U_{t_0-1}^{'}$ and $U_{t_0-1}^{''}$ detect the same nucleus when $U_{t_0-1}^{'}$ and $U_{t_0-1}^{''}$ are tracked by the same unit U_{t_0-2}. ECM determines that $U_{t_0-1}^{'}$ and $U_{t_0-1}^{''}$ detect different nuclei when either or both of $U_{t_0-2}^{'}$ and $U_{t_0-2}^{''}$ are singular units. When both $U_{t_0-2}^{'}$ and $U_{t_0-2}^{''}$ are not singular units, ECM finds singular units at a time point $t_0 - 3$ to complete this check. In this manner, ECM uses singular units at the earlier time points than t_0 until the completion of this check.

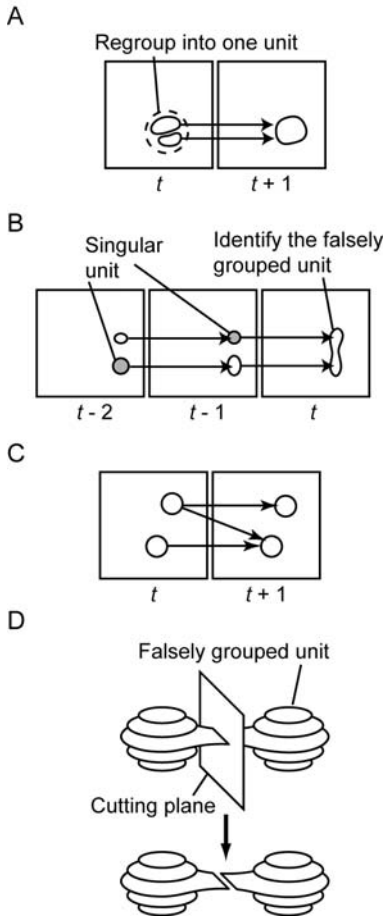

Figure 3.8 Overview of the error-correction module.

After the check whether $U^{'}_{t_0-1}$ and $U^{''}_{t_0-1}$ detect the same nucleus or not, ECM starts to discriminates the detected error as the error (1), (2) and (3), depending on whether U_{t_0} is a singular unit or not. When $U^{'}_{t_0-1}$ and $U^{''}_{t_0-1}$ detect different nuclei, ECM discriminates the error as the error (2) if U_{t_0} is not a singular unit, or as the error (3) if U_{t_0} is a singular unit. When $U^{'}_{t_0-1}$ and $U^{''}_{t_0-1}$ detect the same nucleus, ECM discriminates the error as the error (1) regardless of whether U_{t_0} is a singular unit or not.

After the discrimination of the error (1), (2) and (3), ECM corrects the detected error. For the error (1), ECM re-groups nuclear regions involved in $U^{'}_{t_0-1}$ and $U^{''}_{t_0-1}$ into a single unit. For the error (2), ECM cuts U_{t_0} using a cutting plane and makes two units which should be tracked by $U^{'}_{t_0-1}$ and $U^{''}_{t_0-1}$ respectively; the cutting plane is determined such that its normal is the line segment between the centroids of $U^{'}_{t_0-1}$ and $U^{''}_{t_0-1}$, and the cutting position is determined as the position where the size

of the cross-section of U_{t_0} become the smallest. For the error (3), ECM removes the tracking pathway of either between U'_{t_0-1} and U_{t_0} or between U''_{t_0-1} and U_{t_0}. The determination of removed pathway is as follows: ECM calculates the number of pixels shared by image regions in each focal plane involved in U'_{t_0-1} and U_{t_0}. Similarly, ECM calculates that of U''_{t_0-1} and U_{t_0}. After these calculations, ECM determines that the tracking pathway between units whose number of shared pixels is smaller than that of the other two units should be removed.

3.2.4.2 Detection of the singular unit

I empirically found that the nuclei that are not in the process of cell division are mostly detected by singular units. The 3D shapes of these nuclei look sphere (0 μm, in Figure 3.4). Thus, I expected to detect singular units, if spherical units are detected. To detect spherical units, I introduced two ratios which measure the sphericity of unit; one is defined as a ratio of the number of pixels in regions that are part of a sphere to the ideal number of pixels that are part of the sphere, and the other is defined as a ratio of the number of pixels in regions not part of the sphere to the ideal number of pixels forming part of the sphere. The radius of the sphere is determined as the radius of the minimal enclosing circle (Welzl, 1991), and its center is determined as the centroid of a special region (as described follows) in each unit. The special region is determined as the largest one in the middle focal plane or planes among all the focal planes in each unit; a single focal plane is used when the number of focal planes in the unit is odd, or two focal planes are used when the number of focal planes in the unit is even. I searched the thresholds for these two ratios to detect every error in tracking trajectories (N = 5). I found that every merged unit was detected when the former ratio was larger than 0.37 and the latter ratio was smaller than 0.05. Therefore, ECM determines such units as singular units. Besides, GUI has been implemented in ECM, to enable a manual detection of singular units in case singular units are not enough to detect all merged units in a tracking trajectory.

3.2.5 Required time for measuring a CDP

To examine whether the system reduces the time and labor in the measurement of CDP, I compared the required times of the system and human for obtaining a CDP from a set of 4D DIC microscope images of *C. elegans* embryo from one- to 24-cell stages (Table 3.1). The system took about 2 hours to produce low-entropy regions. Because human would not be able to objectively produce low-entropy regions, human's required time for production of low-entropy regions was not measured (imaginably, the time would be much more than 2 hours). The system took about 25 minutes (including 10 min for manual operations to trigger the forward and backward trackings) to remove non-nuclear regions from low-entropy regions, and human took more than 50 hours to remove non-nuclear regions from low-entropy regions. The system took about 12 min (including the error

correction) to track units, and human took more than 6 hours to track units in which a human used a mouse, clicked nuclear regions to make units and related a tracker- and tracked-units (not including the error correction).

Table 3.1 Required time for measuring a cell division pattern of wild-type embryo from one- to 24-cell stages

Task	System	Human
Production of low-entropy regions	2 h	
Removal of non-nuclear regions	25 min	> 50 h
Tracking of units	12 min	> 6 h

3.2.6 Verification of this system

Figure 3.2 A part of a cell division pattern from 2- to 3-cell stages of a wild-type embryo

Time point	From (unit id)	This (unit id)	x (μm)	y (μm)	z (μm)
30	29000	30000	24.9	27.9	10.8
30	29001	30001	44.0	35.2	10.5
31	30001	31000	41.2	37.5	11.0
31	30000	31001	26.5	24.2	12.6
32	31000	32000	40.1	38.5	11.5
32	31001	32001	26.0	24.1	11.7
33	32001	33000	27.2	24.1	11.4
33	32000	33001	39.8	38.1	12.1
34	33000	34000	28.3	23.8	11.5
34	33001	34001	38.7	38.3	12.0
35	34000	35000	20.6	24.9	10.7
35	34001	35001	36.8	37.9	12.0
35	34000	35002	35.7	22.9	12.9

The origin of the XY plane was defined as the top left corner of the image. The origin of the Z axis was defined as the first focal plane of the set of images of 4-dimensional differential interference microscope.

To verify whether this system can measure CDP, I applied multiple number of CDPs (N = 23) of wild-type embryos to this system. The system measured a CDP from one- to 24-cell stages for each set of 4D DIC microscope images. Each entry in CDP consisted of a time point, tracker unit's ID, tracked unit's ID, and the 3D position of the tracked unit (Table 3.2). To confirm that the resulted CDP was proper, I checked about following two matters. The first matter was whether each unit was properly produced after the measurement of CDP. This matter checked whether at least but no more than one unit was produced for each nucleus at each time point. The second matter was whether units were properly tracked. This matter checked whether nuclei of tracker unit and tracked unit were the same (if in the process of cell division, a mother nucleus and its daughter nucleus were regarded as the same nucleus). Checking by looking through every image one by one (the number of

images was about 154,560; each set of images consisted of about 6,720 images), I confirmed that all CDPs from one- to 24-cell stages were proper about both matters (Table 3.3).

Table 3.3 Verification of measured cell division patterns from one- to 24-cell stages of wild-type embryos

Image set	Proper
Set 1	Y
Set 2	Y
Set 3	Y
Set 4	Y
Set 5	Y
Set 6	Y
Set 7	Y
Set 8	Y
Set 9	Y
Set 10	Y
Set 11	Y
Set 12	Y
Set 13	Y
Set 14	Y
Set 15	Y
Set 16	Y
Set 17	Y
Set 18	Y
Set 19	Y
Set 20	Y
Set 21	Y
Set 22	Y
Set 23	Y

"Y" means that the cell division pattern from 1- to 24-cell stages was proper.

3.2.7 Comparison of CDPs of wild-type embryo with those of *par-1* embryos

To demonstrate a possibility of a quantitative phenotype analysis of CDPs, I compared CDPs of wild-type embryos with those of mutant embryos. For the demonstration, I used *par-1* mutant that is known to show different phenotypes in timing of cell divisions and size of cells in 2-cell stage from those of wild-type embryo (Kemphues *et al.*, 1988). First, I focused on the timing of cell divisions. In the wild-type embryo, the anterior cell in the 2-cell stage (celled AB) always divides earlier than the posterior cell (called P_1) does (Deppe *et al.*, 1978). In the 4-cells stage, AB's daughter cells (called ABa and ABp) always divide earlier than P_1's daughter cells (called EMS and P_2) (Deppe *et al.*, 1978). On the other hand, in *par-1* embryo, cells in 2-cell and 4-cell stages divide synchronously (Kemphues *et al.*, 1988). Therefore, if the time period from the time point at which the 2-cell-stage embryo started dividing to the time point at which the embryo became 4-cell stage was measured, it was expected that the time period of wild-type should be shorter than that of *par-1*. Similarly, if the time period from time point at which the 4-cell-stage embryo started dividing to the time point at

which the embryo becomes the 8-cell stage was measured, it was also expected that the time period of wild-type should be shorter than that of *par-1*. Thus, I used CDPs of wild-type and *par-1* embryos, measured those time periods of wild-type embryos (N = 23) and *par-1* embryos (N = 9), and compared them statistically. In this comparison, the normality among time periods was checked by the Shapiro-Wilk's normality test. If the normality was not rejected, the significance was examined by the Student's *t* test; otherwise, it was examined by the Mann-Whitney's U test. From 2- to 4-cell stages, I found that the time period of wild-type was not significantly shorter than that of *par-1* (P_t > 0.9 in Table 3.4). On the other hand, from 4- to 8-cell stages, I found that the time period of wild-type was significantly shorter than that of *par-1* (P_u < 0.0001 in Table 3.4).

Table 3.4 Time periods between cell stages in wild-type and *par-1* embryos

Cell stage	wt (time point ± sd)	*par-1* (time point ± sd)	Significance
2 - 4	−0.33 ± 2.60	−0.39 ± 2.73	$P_t > 0.9$
4 - 8	12.4 ± 2.68	5.22 ± 2.15	$P_u < 0.0001$

P_t was obtained by the Student's *t* test. P_u was obtained by the Mann-Whitney's U test. The *t* test was used when the distribution was assumed to be a normal distribution (by the Shapiro-Wilk test); otherwise the U test was used.

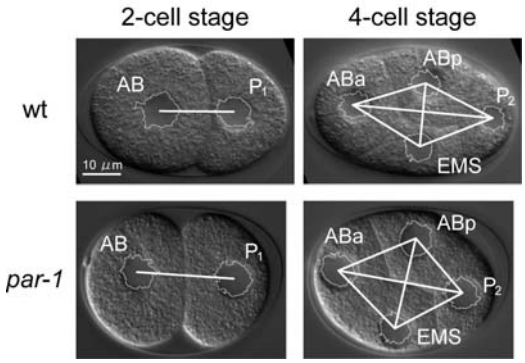

Figure 3.9 Images of wild-type and *par-1* embryos in 2- and 4-cell stages.

Next, I focused the size of cells, AB and P_1, in wild-type and *par-1* embryos. The size of AB is larger than that of P_1 in wild-type, but they are almost the same in *par-1* (Kemphues *et al.*, 1988) (Figure 3.9). According to this, it was expected that this difference in cell size should affect the arrangement of cells in the 4-cell-stage embryo. Thus, I used CDPs of wild-type (N = 23) and *par-1* (N = 9), calculated the distance between centroids of nuclei, averaged each distance in wild-type embryos and in *par-1* embryos respectively, and compared the averaged distances. Consequently, I found that the distances between ABa and ABp and between ABp and EMS in wild-type embryos were significantly shorter than those in *par-1* (P < 0.01 in Table 3.5).

Table 3.5 Comparison of distance between nuclei of 4-cell stage in wild-type and *par-1* embryos

Distance	wt (ave) (μm ± sd)	*par-1* (ave) (μm ± sd)	Significance
ABa-ABp	19.8 ± 1.0	21.2 ± 1.4	$P_u < 0.01$
ABa-EMS	21.5 ± 1.2	21.0 ± 1.8	$P_t > 0.4$
ABa-P_2	36.5 ± 1.2	35.2 ± 2.1	$P_t > 0.09$
ABp-EMS	18.3 ± 1.3	21.6 ± 2.0	$P_t < 0.001$
ABp-P_2	19.9 ± 0.9	20.5 ± 1.1	$P_t > 0.1$
EMS-P_2	21.0 ± 1.6	20.1 ± 1.9	$P_t > 0.2$

P_t was obtained by the Student's t test. P_u was obtained by the Mann-Whitney's U test. The t test was used when the distribution was assumed to be a normal distribution (by the Shapiro-Wilk test); otherwise the U test was used. Distances were measured at the middle time point of the 4-cell stage of each embryo.

3.3 Discussion

3.3.1 Advantage of this system

I consider that this system has three major advantages. The first advantage is that this system objectively measures the positions of nuclei in a set of 4D DIC microscope images. Because the positions of nuclei have been measured by eye observation (Sulston *et al.*, 1983; Schnabel *et al.*, 1997; Heid *et al.*, 2002), the measured positions of nuclei have been affected by human's subjectivity. To eliminate such subjectivity, in this system, tasks to measure positions of nuclei have been automated. The nuclear detection is automated in NDM that uses NDS (Hamahashi *et al.*, 2005). Identification of 3D regions of nuclei is automated in NLM introducing an idea of unit that groups nuclear regions detecting the same nucleus (section 3.2.3). If errors present in making and tracking units, ECM automatically corrects errors (section 3.2.4). Though this system needs some manual operations, the human subjectivity in such operations has little affect on the objectivity in measuring positions of nuclei. In NDM, human selects nuclear regions at the first and last time points of each set of 4D DIC microscope images to trigger the forward and backward trackings. After this manual selection, nuclear regions are selected from whole low-entropy regions at those time points by objectively examining the overlap of low-entropy regions (section 2.2.6, section 2.2.7 and section 2.2.8). In NLM, human also selects nuclear regions at the first time point of each set of 4D DIC microscope images to trigger the step 1 that makes units each of which groups nuclear regions detecting the same nucleus (section 3.2.3). In this step, after the manual selection, units are made by objectively examining the overlap of nuclear regions. Consequently, all processes in relation to the measurement of nuclear positions are objectively operated; this system can objectively measure the positions of nuclei.

The second advantage is that this system reduces the time and labor in the measurement of CDP. Because CDP has been measured manually (Sulston *et al.*, 1983; Schnabel *et al.*, 1997; Heid *et al.*, 2002), the measurement has required a lot of time and labor. To address this problem, most of tasks in measurement of CDP have been automated. The required time of this system was about 160 minutes to measure a CDP, but that of human was more than 50 hours (section 3.2.5). Though this system needed manual operations to trigger the forward and backward trackings in NDS and to trigger the tracking of units, these manual operations took about 10 minutes (section 3.2.5). These results indicate that the system solves the problem of time and labor in the measurement of CDP.

The third advantage is that this system measures the timing of cell division (the precise timing of cell division is difficult to be measured by this system, which is a drawback discussed in the section 3.3.2). Yasuda *et al.*'s system (Yasuda *et al.*, 1999) is hard to measure the timing of cell division. Their system detects nuclei with two processes, similarly to my system; one is the production of image regions that are candidates of nuclear regions, and the other is the selection of nuclear regions from candidates. In this selection process, Yasuda *et al.*'s system selects nuclear regions using the roundness of candidates. Thus, the nuclear regions, detecting nuclei that are in the process of cell division, can not be selected by their system, because the shapes of such nuclei often become long (320 s in Figure 2.1B). If the nucleus that is in the process of cell division is not detected, the timing of cell division can not be measured. To measure the timing of cell division, this system has been designed to detect nuclei that are in the process of cell division. In the detection of nuclei, NDM uses NDS (Hamahashi *et al.*, 2005) which can detect nuclei that are in and not in the process of cell division; in the selection of nuclear regions, NDM does not use the shape of nuclear regions for a criterion of the selection, but it tracks the nuclear regions examining whether nuclear regions overlap or not. NLM makes units and tracks them, which is independent of whether a nucleus is in or not in the process of cell division. Consequently, my system can measure the timing of cell division.

3.3.2 Drawback of this system

The major drawback of this system is a difficulty of measuring the precise timing of cell division. Though this system told the difference of time periods from 4- to 8-cell stages (about 9 minutes) among wild-type and *par-1*, it did not tell the difference from 2- to 4-cell stages (about 1 minute) (Table 3.4); the timing of cell division of AB was measured earlier than that of P_1 in several sets of 4D DIC microscope images (8/23). Because of the limitation of experimental environments, the time interval between time points of 4D DIC microscope images was settled as 40 seconds. This limitation was based on the maximum performance of the microscope used in this system, to record an embryo into multi-focal images of 56 focal planes with a distance of 0.5 μm between two focal planes at each time point. Besides, this system defines the timing of cell division as the time point

when a unit tracked two units, which made the measured timing imprecise. During the tracking process, when a nucleus was in the process of cell division, sometimes a unit once tracked two units, and the two units tracked the same unit. The timing of cell division was therefore determined when a unit finally tracked two units. Thus, the measured timing of cell division became vague and was hard to match the precise timing at which actually what occurs in the process of cell division. This problem would be resolved by shortening the interval of time points in recording the 4D DIC microscope images and changing the threshold value of local image entropy to produce more broken nuclear regions than the current NDM does.

3.3.3 Measurable cell stage exceeding that of Yasuda *et al.*'s system

The measurable cell stage of my system exceeds that of Yasuda *et al.*'s system (Yasuda *et al.*, 1999); my system can measure CDP from one- to 24-cell stages (Table 3.3), but their system is hard to measure CDP after 8-cell stage. Though their system can track nuclear regions whose detecting nuclei are not in the process of cell division, it can not track nuclear regions whose detecting nuclei are in the process of cell division, because it can not detect such nuclei (as described in the previous paragraph). When a nucleus is in the process of cell division, their system focuses on an nuclear region at the final time point among all nuclear regions which have been already tracked as detecting the same nucleus, regards the focused region as the region detecting a mother nucleus, and searches the nearest-neighbor nuclear regions as the regions detecting daughter nuclei, using the 3D Euclidean distance and the time points between nuclear regions. This method would be expected to become hard to track nuclei as the embryo grows. For example, in the 4-cell-stage wild-type embryo, new four cells (called ABal, ABar, ABpl and ABpr) are born almost synchronously after divisions of ABa and ABp. About 7 minutes later, EMS divides and new two cells (called MS and E) are born. Then, about 9 minutes later, ABal, ABar, ABpl and ABpr divide almost synchronously. (The timings of cell divisions described here were measured in my experiments; they are defined as the timing when a unit tracks two units in a tracking trajectory. Each timing was the averaged value of wild-type embryos (N = 23).) In this manner, as the embryo grows and the number of cells increases, more cells divide almost at the same time and the distance between nuclei gets shorter, so that Yasuda *et al.*'s system become harder to infer the nearest-neighbor nuclear regions detecting daughter nuclei from a nuclear region detecting a mother nucleus. To get rid of this problem, this system has been designed to track units (nuclei) successively along a time line without giving up detecting nuclei that are in the process of cell division. NDM in this system uses NDS (Hamahashi *et al.*, 2005) which can detect all nuclei that are in and not in the process of cell division from one- to 24-cell stages. Thus, NLM can make units that detect nuclei that are in the process of cell division. In the process of tracking units, if the nucleus is in the process of cell division, the nuclear region detecting a mother nucleus whose shape is a long shape overlaps the nuclear region detecting a

daughter nucleus. Thus, to track units, NLM does not have to infer nuclear regions detecting daughter nuclei at several time points later from a nuclear region detecting their mother nucleus, but does check whether nuclear regions in adjacent time points overlap or not. This method would allow tracking units if the number of cells increases (more than 8-cell stage) and many cells divide at almost the same time. According to the difference of tracking methods, NLM would measure CDP until the longer cell stage than Yasuda *et al.*'s system does.

The maximum cell stage that my system can measure would be currently limited until about the 44-cell stage. This limitation comes from the limitation of nuclear detection using NDS (the limitation of nuclear detection is discussed in section 2.3.4). The system presented in this chapter has GUIs that enable measuring a CDP if the automated measurement fails. Thus, the maximum cell stage of nuclear detection is the limitation of measurable cell stage of this system. As discussed in section 2.3.4, the limitation of nuclear detection would be overcome.

3.3.4 Applicability

This system has already been applied to the other researches, in which the objectivity and productivity are required. The high objectivity and productivity of this system are used in a large-scale gene-knockout analysis of CDPs in *C. elegans* (Onami *et al.*, 2001; the related works has been presented by Onami S., Urai M., Masuda E., Nagai Y., Oguro T., Kimura A. and Hamahashi S. at a conference named "The 27th Annual Meeting of the Molecular Biology Society of Japan" held in 2004, by Kyoda K., Hamahashi S., Urai M., Masuda E., Nagai Y., Oguro T. and Onami S. at a conference named "The 15th Biennial International *C. elegans* Conference" held in 2005 and by Kyoda K., Hamahashi S., Urai M. and Onami S. at a conference named "The 28th Annual Meeting of the Molecular Biology Society of Japan" held in 2005). The analysis using the objective and productive measurement of CDPs will provide new opportunities for bioinformatics in studies of the development of multicellular organisms (Braun *et al.*, 2003).

When the shapes and/or positions of nuclei themselves are the targets to be measured, this system should be carefully used. Because the angle makes a substantial artifact in DIC microscope images (Preza *et al.*, 1999), a consideration of the DIC shear angle would be required to calculate the precise 3D shape and/or position of a nucleus detected by nuclear regions.

When the cell fusion is followed, this system will need an additional extension. This system follows cell divisions along a time line using an idea of unit that detects 3D regions of each nucleus (3.2.3). This idea may also allow following cell fusions. However, the current system is hard to follow them because ECM confuses the cell fusion and the errors occurred in step 1 and 2 in the NLM (explained

in section 3.2.4). ECM detects errors when a unit tracks more than two units in a tracking trajectory (section 3.2.4.1). The cell fusion will cause the same situation in tracking trajectory. To follow the cell fusion, the more sophisticated idea of error correction will be required than that of current system.

3.4 Summary

In this chapter, I presented a system that objectively and productively measures a CDP in *C. elegans* embryo. This system consists of NDM, NLM and ECM. NDM is developed base upon NDS (Chapter 2). NLM identifies the 3D region of each nucleus by unit that groups nuclear regions, tracks units along a time line, and outputs a tracking trajectory that is the measured CDP (section 3.2.3). ECM automatically corrects nuclear regions to make each nuclear region detect a single nucleus (section 3.2.4). This system allows measuring CDP from one- to 24-cell stages (Table 3.3). This system can detect nuclei that are both in and not in the process of cell division, so that this system can measure the timing of cell division (Table 3.4). Because most of tasks in this system have been automated, this system objectively and productively measures a CDP. In case automated tasks fail, GUIs enable manually assisting the automated tasks to continue the measurement.

Methods

Preparation of 4D DIC microscope images of *C. elegans* embryos

The Bristol N2 *C. elegans* was cultured under standard conditions (Brenner, 1974). An embryo immediately after fertilization (before meeting of the female and male pronuclei) was dissected from a hermaphrodite and mounted on a 2% agar pad on a glass slide, covered with a coverslip, and sealed with petroleum jelly. Nomarski DIC microscope images were obtained using a Leica DMRE microscope equipped with an HCX PL APO 100×/1.40 NA objective, whose illumination intensity and objective-side Wollaston prism were adjusted to obtain images of the same quality. Digital images of 600 × 600 pixels with 256 gray levels (0.1 μm per pixel) were recorded with an ORCA CCD Camera (Hamamatsu Photonics), and the recording system was controlled by IP Lab 3.5 software (Scanalytics). Digital images of the developing embryo were recorded at 22°C in 56 focal planes, with a distance of 0.5 μm between two focal planes, and a set of 56 focal plane images was recorded every 40 s for 2 h.

Hardware and software environment

The task in NDM to produce low-entropy regions was implemented in a Beowulf-class PC cluster (Sterling *et al.*, 1995) consisting of 48 nodes, each of which used a 2 GHz Intel Pentium 4 processor,

1 GB of SDRAM memory, and a 100 Base-TX Ethernet card. Parallel Virtual Machine software (Sunderam, 1990) was used for communications between the nodes. In the production of low-entropy regions, a window of 10 × 10 pixels was used to calculate the local image entropy (Handmann *et al.*, 2000), and a value of 175 was used for the threshold of local image entropy. To remove non-nuclear regions by the forward and backward trackings, the minimum overlap ratios of 73% and 8% were used for T_f and T_t (section 2.2.8) respectively. The tasks in NDM to select nuclear regions from low-entropy regions, in NLM and in ECM were implemented in a single processor PC that used a 2.2 GHz Intel Pentium 4 processor and 1 GB of RDRAM memory. All programs were written in programming languages C and C++.

Chapter 4 Derivative system: a system measuring the spindle orientation

4.1 Introduction

The spindle orientation during the cell division provides important information to understand the development of embryos. The spindle forms during cell division and the cell divides along the spindle axis. In *C. elegans* embryo, the germ-line cells divide along the anterior-posterior axis, whereas the somatic cells divide orthogonally to the previous division (Riddle *et al.*, 1997). The pattern of cell divisions from one-cell stage to the adult is roughly the same among the wild-type embryos (Sulston *et al.*, 1983). Many mutants were identified in which the pattern of cell divisions is remarkably different from that in wild-type. Spindle orientations are measured in many different mutant embryos (Kemphues *et al.*, 1988; Cheng *et al.*, 1995; Watts *et al.*, 1996).

The spindle orientation has been manually measured at a single time point (Sulston *et al.*, 1983; Cheng *et al.*, 1995; Watts *et al.*, 1996; Schnabel *et al.*, 1997). Two methods have been used to measure the spindle orientation, namely that using positions of nuclei and that using positions of centrosomes. The orientation of cell division axis, which is parallel to the spindle orientation, was measured using a line connecting the positions of daughter nuclei. In this method, nuclei were visualized in a living embryo through a Nomarski differential interference contrast (DIC) microscope (Nomarski and Weill, 1955) and the positions of the nuclei were determined manually at the birth of these nuclei (Sulston *et al.*, 1983; Schnabel *et al.*, 1997). The spindle orientation was measured using a line connecting the positions of centrosomes. In this method, centrosomes were visualized either by using a DIC microscope (Watts *et al.*, 1996; Gomes *et al.*, 2001) or by immunostaining (Cheng *et al.*, 1995; Watts *et al.*, 1996), and the positions of centrosomes were determined manually at a single time point. Because the positions of nuclei or centrosomes are determined manually, the objectivity and productivity of the measurement are low in these methods. In addition, because the spindle orientation has been measured in a single time point in these methods, the time-transition of the spindle orientation remains to be measured.

To detect spindles, I considered that NDM (section 3.2.2) would be an appropriate method; NDM is involved in the CDP measurement system (Chapter 3) and detects nuclei in DIC microscope images of *C. elegans* embryos. NDM uses the local image entropy (Handmann *et al.*, 2000) to discriminate

the image texture of nuclei from that of cytoplasm. Because the image texture of spindle is similar to that of nucleus (Figure 4.1, see also Figure 2.1B), and because NDM can detect nuclei that are in the process of cell division, NDM detects not only nuclei but also spindles. GUI, which is implemented in NDM, allows handling a specific nuclear region. In addition, because NDM almost automatically detects spindles, the objectivity and productivity of the detection of spindles are high. Consequently, NDM is an appropriate method to be used in developing a system that objectively measures the spindle orientation.

In this chapter, I present a system that objectively measures the spindle orientation during cell divisions in *C. elegans* embryo. I have developed this system (Hamahashi and Onami, 2005) using the CDP measurement system (Hamahashi *et al.*, 2006) (explained in Chapter 3) and the regression line (Montgomery and Peck, 1982). The CDP measurement system was used to objectively detect spindle in DIC microscope images, and the regression line was used to objectively calculate the orientation of nuclear region that detected the spindle (hereafter a nuclear region that detects a spindle is called a *nuclear region of spindle*). The development of this system shall demonstrate the applicability of the CDP measurement system to research programs that require the objectivity of nuclear detection in *C. elegans* embryo.

4.2 Results

4.2.1 Spindle orientation measured by regression line

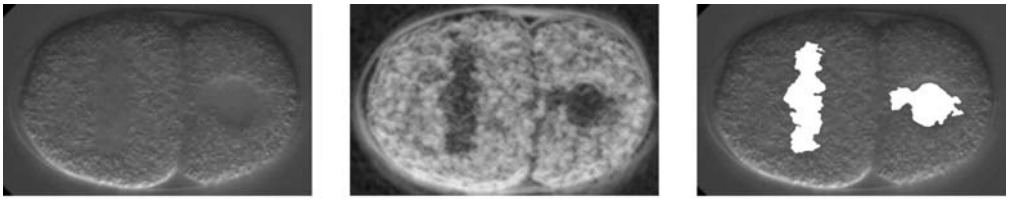

Figure 4.1 Detection of spindles in a *Caenorhabditis elegans* embryo. In the middle panel, the darker color represents the lower local image entropy and the brighter color represents the higher local image entropy. In the right panel, the white regions show nuclear regions of spindles.

The spindle starts to form at prometaphase of cell cycle, when the centrosomes move at the spindle poles (Figure 4.1). The spindle orientation was defined using the line connecting two positions of centrosomes at the spindle poles. To measure the spindle orientation using nuclear regions, I assumed that the orientation of nuclear region of spindle should correlate with the line connecting

two positions of centrosomes. With this assumption, the spindle orientation was calculated using the regression line of nuclear region of spindle (Figure 4.2).

The calculation of the angle of regression line for a nuclear region is as follows: All pixels in a nuclear region of spindle were used to calculate the angle of the regression line. When S_{xx} is the sum of squared errors in x and S_{xy} is the sum of cross-products of x and y, S_{xx} and S_{xy} are described as follows: $S_{xx} = \sum (x - \bar{x})^2$ and $S_{xy} = \sum (x - \bar{x})(y - \bar{y})$, where $\bar{x} = \sum x / N$, $\bar{y} = \sum y / N$ and N is the number of data (number of pixels in the nuclear region). The angle of the regression line is calculated as S_{xx}/S_{xy} and the angle θ (degree) is described as follows: $\theta = \arctan(S_{xy} / S_{xx})$.

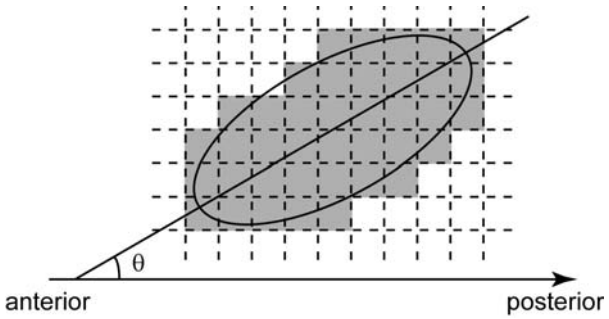

Figure 4.2 Orientation of nuclear region of spindle. The squares in gray show a nuclear region. The line with the angle θ to the anterior-posterior axis is the regression line.

4.2.2 Production of nuclear regions of spindles using a system measuring CDP

Sets of single-focal time-lapse DIC microscope images of *C. elegans* embryo were applied to NDM (Hamahashi *et al.*, 2006) (Chapter 3), and image regions consisting of pixels whose local image entropy is lower than the threshold were produced. The window size for calculating the local image entropy was 10 × 10 pixels. The value of threshold to binarize the local image entropy was 95 for DIC microscope images of wild-type embryos and 110 for those of *par-2(RNAi)* and *par-3(RNAi)* embryos. Nuclear regions were automatically selected from the produced regions using an object-tracking algorithm (Hamahashi *et al.*, 2005) (Chapter 2). If the object-tracking algorithm falsely selected image regions of cytoplasm, I manually removed these regions through GUI in NDM (Chapter 3). The time point 0 of each set of images was set to the earliest time point after the centrosomes' movement.

4.2.3 Spindle orientations in wild-type *C. elegans* embryo

I measured the spindle orientation of wild-type *C. elegans* embryos using the system. In this work, I focused on the second cell divisions of embryo because the entire shape of the spindles during the

second cell divisions, in which the embryo grows from 2-cell to 4-cell embryo, can be observed in a single focal plane of the DIC microscope. During the second cell divisions, the spindle in the anterior cell (called AB) forms transversely along the anterior-posterior (called AP) axis, whereas the spindle orientation in the posterior cell (called P_1) is parallel to the AP axis (Riddle *et al.*, 1997). I recorded DIC microscope images of wild-type embryos and examined whether the entire shape of spindles were observed. In the most of recorded sets (8/10) of DIC microscope images, both AB spindle and P_1 spindle were observed in a single focal plane. In the other sets (2/10), one of the poles of AB spindle went to a different focal level, so that the entire spindle was not observed in a single focal plane.

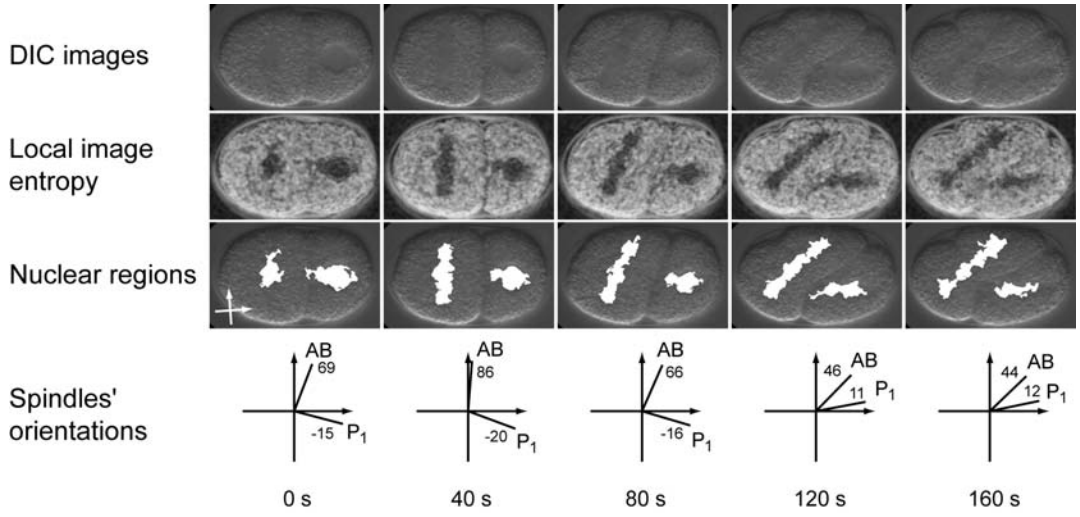

Figure 4.3 Spindle orientations in a wild-type embryo. Panels in the top row show time-series DIC images of the same wild-type *Caenorhabditis elegans* embryo. Each panel in the second row shows local image entropy corresponding to the DIC image at the top panel in each column. The brighter color represents the higher local image entropy. White regions in the third row show nuclear regions of spindles. Measured orientations of spindles are shown with angles (degree) and lines in the bottom row in each column. The axes of reference orientation to calculate the spindle orientation are shown as white arrows in the third top panel at time 0 s. The anterior-posterior axis of the reference orientation is parallel to a line connecting centroids of nuclear regions of AB and P_1 at the last time point before spindle formations.

I selected DIC microscope images in which the entire shape of spindles were observed, applied these images to the NDS, and obtained nuclear regions of spindles (Figure 4.3). The system presented in this chapter calculated the angle of the regression line of these nuclear regions (Figure 4.3). I obtained the angles of the spindle orientations during the second divisions of embryo's development (Figure 4.3). For example, I obtained 86° (40 s in Figure 4.3) for the AB spindle that is known to be

transverse along the AP axis, and –20° (40 s in Figure 4.3) for the P_1 spindle that is known to be parallel to the AP axis. From the viewpoint of the measurement system, I examined the reproducibility of values measured by this system. I confirmed that the measured values were completely the same when I measured the spindle orientation many times (more than 10 times) at the same time point using the same set of images.

4.2.4 Spindle orientations in RNAi embryos

To examine if this system can measure the spindle orientations in mutant embryos, I measured spindle orientations of *par-2(RNAi)* and *par-3(RNAi)* embryos using this system. The spindle orientations in these embryos are different from that in wild-type embryo (Kemphues *et al.*, 1988; Gomes *et al.*, 2001). In the *par-2(RNAi)* embryo, both AB and P_1 spindles are transverse along the AP axis (Kemphues *et al.*, 1988). In the *par-3(RNAi)* embryo, both AB and P_1 spindles are parallel to the AP axis (Kemphues *et al.*, 1988).

DIC microscope images of *par-2(RNAi)* and *par-3(RNAi)* embryos were recorded and applied to the system. I obtained the angles of the spindle orientations of *par-2(RNAi)* and *par-3(RNAi)* embryos. Figure 4.4 shows results of a *par-3(RNAi)* embryo. In this example, I obtained 23° (0 s in Figure 4.4) for the orientation of AB spindle and 14° (0 s in Figure 4.4) for the orientation of P_1 spindle.

4.2.5 Time-transition of spindle orientation

Figure 4.5 shows the time-transitions of the spindle orientations during the second divisions of embryo's development in wild-type, *par-2(RNAi)* and *par-3(RNAi)* embryos. For each condition of embryos, the spindle orientations were measured in five embryos and the results were averaged in each time point. I found clear differences in time-transitions among these embryos. In wild-type embryos, the orientation of AB spindle was about 85° (transverse to the AP axis) and that of P_1 spindle was about –5° (parallel to the AP axis) at the beginning of cell division. As the cell division proceeded, the orientation of AB spindle decreased and the P_1 orientation increased, so that orientations gradually became nearly parallel. In *par-2(RNAi)* embryos, orientations of both AB and P_1 spindles were about 89° and 91° respectively (almost transverse to the AP axis) at the beginning of cell division, and did not change a lot within 120 s. In *par-3(RNAi)* embryos, orientations of both AB and P_1 spindle were about 2° and 9° respectively (almost parallel to the AP axis) at the beginning of cell division, and did not change a lot within 120 s.

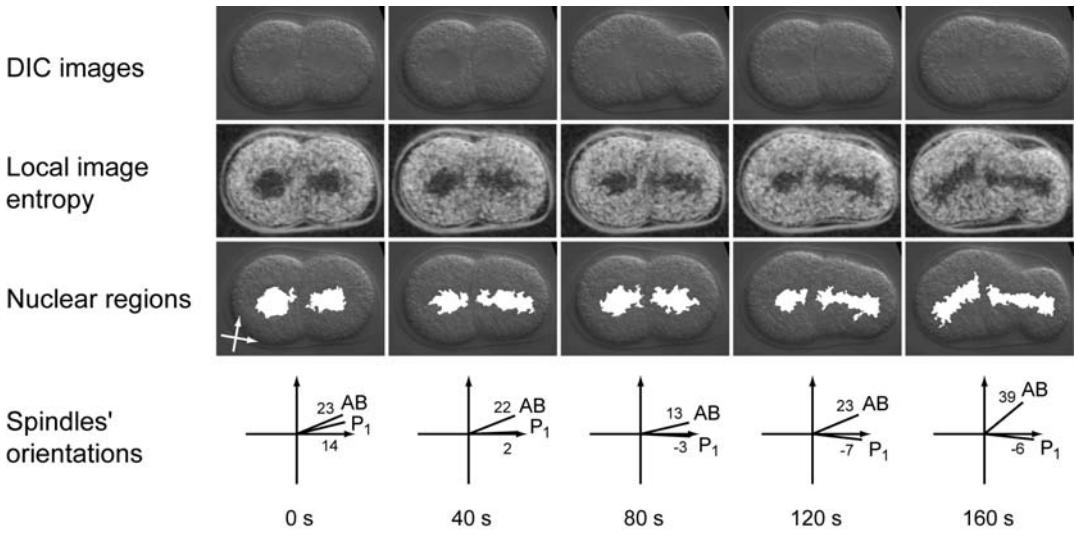

Figure 4.4 Spindle orientations in a *par-3(RNAi)* embryo. Panels in the top row show time-series DIC images of the same *par-3(RNAi)* embryo. Each panel in the second row shows local image entropy corresponding to the DIC image at the top panel in each column. The brighter color represents the higher value of the local image entropy. White regions in the third row show nuclear regions of spindles. Measured orientations of spindles are shown with angles (degree) and lines in the bottom row in each column. The axes of reference orientation to calculate the spindle orientation are shown as white arrows in the third panel at time 0 s. The anterior-posterior axis of the reference orientation is parallel to a line connecting centroids of nuclear regions of AB and P_1 at the last time point before spindle formations.

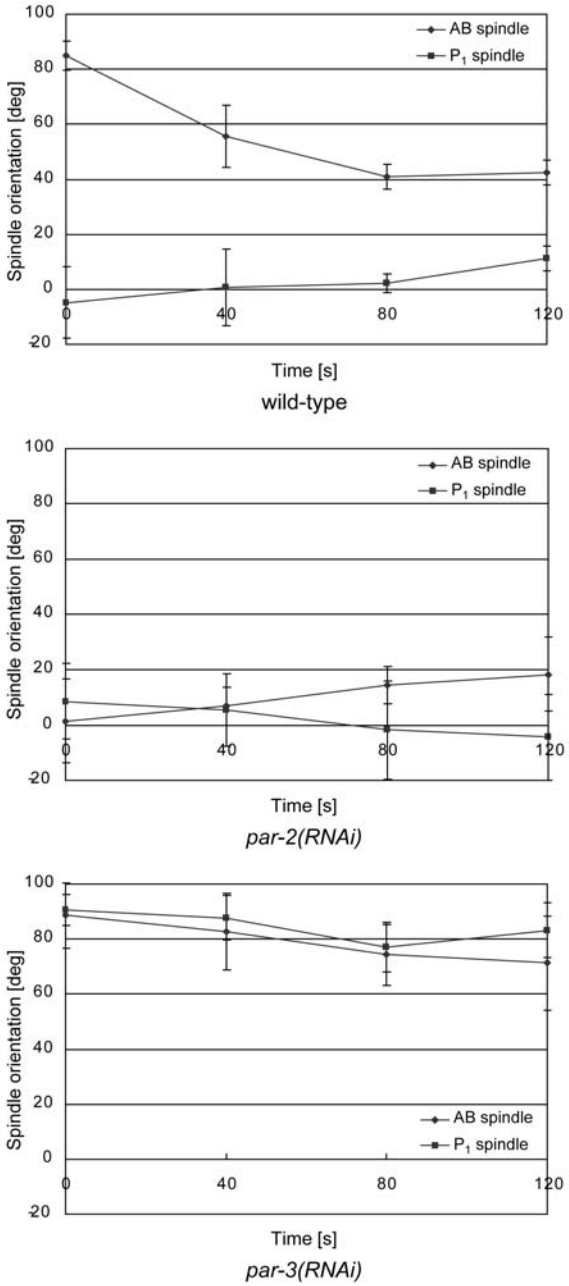

Figure 4.5 Time-transitions of spindle orientations. Time-transitions of spindle orientations in wild-type, *par-2(RNAi)* and *par-3(RNAi)* are displayed. Horizontal value represents the averaged orientation of spindles (N = 5), and the error bar represents the standard deviation. Time point 0 was defined as the time point when all centrosomes in AB and P_1 cell positioned on the cell-division axis.

4.3 Discussion

4.3.1 Advantage of this system

I consider that this system has three main advantages. The first advantage is the high objectivity of the measurement of spindle orientation. The spindle orientation has been manually measured by discriminating the difference of image texture between spindle and cytoplasm in DIC microscope images (Watts *et al.*, 1996; Gomes *et al.*, 2001) or detecting the spindles stained using immunostaining technique (Cheng *et al.*, 1995; Watts *et al.*, 1996), where the objectivity of the measurement has been low. To address this problem, I used NDM (Hamahashi *et al.*, 2006) (Chapter 3) and the regression line (Montgomery and Peck, 1982). NDM can objectively produce nuclear regions of spindles. The regression line can objectively calculate the angle of nuclear region. Because all tasks in the measurement are carried out objectively in this system, I consider that this system can objectively measure the spindle orientation.

The second advantage is the high productivity of the measurement of spindle orientations. The spindle orientation has been measured by manually looking at images one by one to discriminate the image texture of spindle from that of cytoplasm or to determine the positions of centrosomes (Cheng *et al.*, 1995; Watts *et al.*, 1996; Gomes *et al.*, 2001). Because the measurement of spindle orientation has been laborious, the productivity of the measurement has been low. To address this problem, I automated most of tasks in the measurement of spindle orientation. My system used NDM, which automatically produces nuclear regions of spindles, so that the productivity of producing nuclear regions of spindles is high. In addition, my system used the regression line, which automatically calculates the spindle orientation from nuclear regions of spindles. I demonstrated that my system measured spindle orientations in multiple numbers of wild-type, *par-2(RNAi)* and *par-3(RNAi)* embryos (N = 5 for each embryo) (Figure 4.5). These results indicate that my system productively measures the spindle orientations. This productivity will allow a large-scale analysis of spindle orientation. Because of a benefit of 4D DIC microscope system (Hird and White, 1993; Thomas *et al.*, 1996), numbers of DIC microscope images of *C. elegans* embryos can be recorded automatically. In addition, many sets of time-lapse DIC microscope images of RNAi embryos for many genes have been available from an online database (Sönnichsen *et al.*, 2005). Appling these data to my system, a systematic analysis of spindle orientations will become practicable.

The third advantage of my system is that the system enables the analysis of time-transitions of spindle orientations. Although the spindle orientation changes during cell division (Figure 4.5), the spindle orientation has been usually measured at a single time point during cell division (Cheng *et al.*, 1995; Watts *et al.*, 1996; Gomes *et al.*, 2001). Because this system can measure spindle orientation during cell division in a highly automated manner, this system enables the measurement

of time-transitions of spindle orientations (Figure 4.5). Though I demonstrated an analysis of time-transitions using 4 time points (Figure 4.5), this demonstration indicates that the analysis using a lot of time points with a very short time interval would be practical.

4.3.2 Limitation of this system

The limitation of this system is that the current system is applicable to the measurement of 2D spindle orientations. Before developing the system to measure the 3D orientation of spindle, I focused on the 2D orientation of spindle to simplify the problem that was to develop a system measuring the spindle orientation. Because the entire shape of spindle in 2- to 4-cell stages can be viewed in a single focal plane of a microscope, I used these cell stages. The results of this system indicate that this system will be a possible approach to measure the spindle orientation in a *C. elegans* embryo. The 3D orientation of spindle would be measured by a combination of 2D regression lines that are obtained by projections of spindle onto the XY-plane, the YZ-plane and the ZX-plane.

4.4 Summary

In this chapter, I presented a system that measures the spindle orientation in *C. elegans* embryo. Using the CDP measurement system presented in Chapter 3 and the regression line, this system objectively and productively measures spindle orientations during second cell divisions in embryos. The objective and productive measurement of spindle orientations helped to discriminate the differences in phenotypes among wild-type, *par-2(RNAi)* and *par-3(RNAi)*.

Methods

Preparation of DIC microscope images of *C. elegans* embryos

Embryo immediately after fertilization (before meeting of the female and male pronuclei) were dissected from a gonad, placed on a slide coated with 0.01% poly-L-lysine (Sigma) in M9 solution, covered with a coverslip, and sealed with petroleum jelly. DIC images were obtained using a Leica DMRE microscope equipped with a HCX PL APO 100×/1.40 NA objective, whose illumination intensity and objective-side Wollaston prism were adjusted to obtain images of the same quality. Digital images of 600 × 600 pixels with 256 gray levels (0.1 μm per pixel) were recorded with an ORCA CCD Camera (Hamamatsu Photonics), and the recording system was controlled by IP Lab 3.5 software (Scanalytics). Digital images of the developing embryo were recorded at 22°C. The time interval between time points in each set of images was 40 s.

Production of nuclear regions of spindle using NDS

DIC images were applied to NDS (Chapter 2) and nuclear regions were produced. The window size for calculating the local image entropy was 10 × 10 pixels. The value of threshold to binarize the local image entropy was 95 for images of wild-type embryos and 110 for those of *par-2(RNAi) and par-3(RNAi)* embryos.

Chapter 5 Conclusion

5.1 Summary of results

I developed a system that objectively and productively measures a CDP in a *C. elegans* embryo. I have focused the objectivity and productivity of measurement in embryogenesis of *C. elegans* through my work. In this dissertation, I presented three systems that I have developed during my work; the basic system that detects nuclei (NDS) (Hamahashi *et al.*, 2005) (Chapter 2), the main system that measures a CDP (Hamahashi *et al.*, 2006) (Chapter 3) and a derivative system that measures a spindle orientation (Hamahashi and Onami, 2005) (Chapter 4).

The basic system objectively and productively detects nuclei in a set of 4D DIC microscope images of *C. elegans* embryo. This system automatically detects nuclei using a difference in image textures between the nucleus and the cytoplasm in DIC microscope images (section 2.2.1). The difference is distinguished by local image entropy (Handmann *et al.*, 2000) that makes the system applicable to different sets of 4D DIC microscope images without the need of hand-tuning of system's parameters (section 2.2.4 and section 2.3.1). The system first produces nuclear regions and non-nuclear regions (section 2.2.5). Then, this system automatically selects nuclear regions from produced regions using an object-tracking algorithm (Geerts *et al.*, 1987; Lee *et al.*, 1991; Awasthi *et al.*, 1994) (section 2.2.6, section 2.2.7 and section 2.2.8). The use of object-tracking algorithm allows selecting nuclear regions detecting nuclei that are both in and not in the process of cell division, which makes this system possible to detect nuclei that are in the process of cell division (section 2.3.2).

The main system objectively and productively measures a CDP in a *C. elegans* embryo. This system first automatically produces nuclear regions from a set of 4D DIC microscope images using the basic system (section 3.2.2). Then, this system identifies 3-dimensional regions of nuclei using units, and tracks units along a time line to output a tracking trajectory that is the measured CDP (section 3.2.3). If a unit groups inappropriate nuclear regions, this system detects the group and corrects it (section 3.2.4). If this system inappropriately tracks units (nuclei detected by a tracker and a tracked units are different), this system detects this failure and corrects it (section 3.2.4). Because this system can detect nuclei that are both in and not in the process of cell division, this system can measure the timing of cell division (section 3.2.7). This system measures CDP from one- to 24-cell stages. Because most of tasks in this system have been automated, the objectivity and productivity of this system are high.

The derivative system objectively and productively measures a spindle orientation in a *C. elegans* embryo. This system uses NDM (section 3.2.2) to detect spindles and the main system to handle each nuclear region through GUIs (Chapter 3). For the calculation of the spindle orientation, this system uses the regression line (Montgomery and Peck, 1982). The system measures a spindle orientation in second cell divisions in a *C. elegans* embryo (section 4.2.3 and section 4.2.4). Most of tasks in this system have been automated, so that the objectivity and productivity of this system are high.

5.2 Prospects

The systems presented in this dissertation might be applicable to research programs analyzing not only *C. elegans* but also some other animals though the animals are limited. The systems are developed using special features of the embryo. The *C. elegans* embryo is transparent through its life (Wood, 1988), which allows monitoring individual cells by direct observation with a DIC microscope (Nomarski and Weill, 1955). The nuclear detection is allowed by the difference in image textures between the nucleus and the cytoplasm in DIC microscope images (section 2.2.1). The embryos are also transparent in some species, such as zebrafish and sea urchin. Individual cells in these embryos can be monitored by a DIC microscope, where the difference in image textures between the nucleus and the cytoplasm might be usable to distinguish them and my systems might be applied to these animals. Actually, for example, the image textures in sea urchin embryo look similar to those of *C. elegans* embryo (Scott, 1997). On the contrary, embryos in the other most species are not transparent, so that my systems would not be directly applicable to these animals.

The significance of the systems is that they enable objective and productive measurements in embryogenesis in a multicellular organism, *C. elegans*. These objective and productive measurements will allow a large-scale and quantitative phenotype evaluation. Analyses of development often compare CDPs, such as timings or orientations of cell divisions and/or positions of nuclei, among wild-type and RNAi-treated embryos (Fraser *et al.*, 2000; Gönczy *et al.*, 2000; Sönnichsen *et al.*, 2005), where the problems of objectivity and productivity in the measurements are often faced. Because *C. elegans* has about twenty thousand genes (The *C. elegans* Sequencing Consortium, 1998), an manual analysis with eye observation has a limitation. For example, it would be almost impossible that phenotypes of all genes are analyzed based on the assumption that an observer would notice the anomaly at the first place and recognize that anomaly is beyond the range expected as wild-type individual variations. The systems presented in this dissertation enable highly objective and productive measurement of CDPs, so that possible anomalies are all data-logged and

evaluated with statistical significance, instead of relying upon experience of individual observers. The systems presented in this dissertation open the way to the future analysis of multicellular organism in developmental biology.

References

Awasthi, V., Doolittle, K., Parulkar, G. and McNally, J. Cell tracking using a distributed algorithm for 3-D image segmentation. *Bioimaging* 1, 98-112, 1994.

Braun, V., Azevedo, R.B., Gumbel, M., Agapow, P.M., Leroi, A.M. and Meinzer, H.P. ALES: cell lineage analysis and mapping of developmental events. *Bioinformatics* 19, 851-858, 2003.

Brenner, S. The genetics of *Caenorhabditis elegans*. *Genetics* 77, 71-94, 1974.

Cheng, N.N., Kirby, C.M. and Kemphues, K.J. Control of cleavage spindle orientation in *Caenorhabditis elegans*: the role of the genes *par-2* and *par-3*. *Genetics* 139, 549-559, 1995.

Chisholm, A.D. Cell lineage. In *The encyclopedia of Genetics*. (Eds) Brenner, S. and Miller, J.H., Academic Press, San Diego, 1, 302-310, 2002.

Denk, W., Strickler, J.H. and Webb, W.W. Two-photon laser scanning fluorescence microscopy. *Science* 248, 73-76, 1990.

Deppe, U., Schierenberg, E., Cole, T., Krieg, C., Schmitt, D., Yoder, B. and von Ehrenstein, G. Cell lineages of the embryo of the nematode *Caenorhabditis elegans*. *Proceedings of the National Academy of Sciences of the United States of America* 75, 376-380, 1978.

Fire, A. Integrative transformation of *Caenorhabditis elegans*. *EMBO Journal* 5, 2673-2680, 1986.

Fire, A., Xu, S., Montgomery, M.K., Kostas, S.A., Driver, S.E. and Mello, C.C. Potent and specific genetic interference by double-stranded RNA in *Caenorhabditis elegans*. *Nature* 391, 806-811, 1998.

Fraser, A.G., Kamath, R.S., Zipperlen, P., Martinez-Campos, M., Sohrmann, M. and Ahringer, J. Functional genomic analysis of *C. elegans* chromosome I by systematic RNA interference. *Nature* 408, 325-330, 2000.

Geerts, H., De Brabander, M., Nuydens, R., Geuens, S., Moeremans, M., De Mey, J. and Hollenbeck, P. Nanovid tracking: a new automatic method for the study of mobility in living cells based on colloidal gold and video microscopy. *Biophysical Journal* 52, 775-782, 1987.

Gomes, J.E., Encalada, S.E., Swan, K.A., Shelton, C.A., Carter, J.C. and Bowerman, B. The maternal gene *spn-4* encodes a predicted RRM protein required for mitotic spindle orientation and cell fate patterning in early *C. elegans* embryos. *Development* 128, 4301-4314, 2001.

Gönczy, P., Echeverri, C., Oegema, K., Coulson, A., Jones, S.J., Copley, R.R., Duperon, J., Oegema, J., Brehm, M., Cassin, E., Hannak, E., Kirkham, M., Pichler, S., Flohrs, K., Goessen, A., Leidel, S., Alleaume, A.M., Martin, C., Özlü, N., Bork, P., Hyman, A.A. Functional genomic analysis of cell division in *C. elegans* using RNAi of genes on chromosome III. *Nature* 408, 331-336, 2000.

Hamahashi, S. and Onami, S. Objective measurement of spindle orientation in early *Caenorhabditis elegans* embryo. *Genome Informatics* 16, 86-93, 2005.

Hamahashi, S., Kitano, H. and Onami, S. A system for identification of cell division patterns in early embryogenesis of *Caenorhabditis elegans* using image processing and object tracking. *Institute of Electronics, Information and Communication Engineers*, 2006, (accepted).

Hamahashi, S., Onami, S. and Kitano, H. Detection of nuclei in 4D Nomarski DIC microscope images of early *Caenorhabditis elegans* embryos using local image entropy and object tracking. *BMC Bioinformatics* 6, 125, 2005.

Handmann, U., Kalinke, T., Tzomakas, C., Werner, M. and Seelen, W. An image processing system for driver assistance. *Image and Vision Computing* 18, 367-376, 2000.

Heid, P.J., Voss, E. and Soll, D.R. 3D-DIASemb: a computer-assisted system for reconstructing and motion analyzing in 4D every cell and nucleus in a developing embryo. *Developmental Biology* 245, 329-347, 2002.

Hengartner M.O. and Horvitz, H.R. *C. elegans* cell survival gene ced-9 encodes a functional homolog of the mammalian proto-oncogene *bcl-2*. *Cell* 76, 665-676, 1994.

Hird, S.N. and White, J.G. Cortical and cytoplasmic flow polarity in early embryonic cells of *Caenorhabditis elegans*. *Journal of Cell Biology* 121, 1343-1355, 1993.

Jahne, B., Hausecker, H. and Geisler, P. *Handbook of Computer Vision and Applications Volume 2: Signal Processing and Pattern Recognition*. Academic Press, San Diego, 1999.

Kelly, W.G., Xu, S., Montgomery, M.K. and Fire, A. Distinct requirements for somatic and germline expression of a generally expressed *Caernorhabditis elegans* gene. *Genetics* 146, 227-238, 1997.

Kemphues, K.J., Priess, J.R., Morton, D.G. and Cheng, N.S. Identification of genes required for cytoplasmic localization in early *C. elegans* embryos. *Cell* 52, 311-320, 1988.

Kimura, A. and Onami, S. Computer simulations and image processing reveal length-dependent pulling force as the primary mechanism for *C. elegans* male pronuclear migration. *Developmental Cell* 8, 765-775, 2005.

Kirsch, R.A. Computer determination of the constituent structure of biological images. *Computers and Biomedical Research* 4, 315-328, 1971.

Lee, G.M., Ishihara, A. and Jacobson, K.A. Direct observation of brownian motion of lipids in a membrane. *Proceedings of the National Academy of Sciences of the United States of America* 88, 6274-6278, 1991.

Liu, H.S., Jan, M.S., Chou, C.K., Chen, P.H. and Ke, N.J. Is green fluorescent protein toxic to the living cells? *Biochemical and Biophysical Research Communications* 260, 712-717, 1999.

Montgomery, D. and Peck, E. *Introduction to linear regression analysis*. John Wiley & Sons, New York, 1982.

Nomarski, G. and Weill, A.R. Application à la métallographie des méthodes interférentielles à deux ondes polarisées. *Revue de Metallurgie* 52, 121-134, 1955.

Onami, S., Hamahashi, S., Nagasaki, M., Miyano, S. and Kitano, H. Automatic acquisition of cell lineage through 4D microscopy and analysis of early *C. elegans* embryos. In *Foundations of Systems Biology*. (Ed) Kitano, H., MIT Press, Cambridge, Massachusetts, 39-55, 2001.

Otsu, N. A thresholding selection method from gray-level histogram. *IEEE Transactions on Systems, Man and Cybernetics* 9, 62-66, 1979.

Praitis, V., Casey, E., Collar, D. and Austin, J. Creation of low-copy integrated transgenic lines in *Caenorhabditis elegans*. *Genetics* 157, 1217-1226, 2001.

Pratt, W. *Digital Image Processing*. John Wiley & Sons, New York, 1991.

Prewitt, J. Object enhancement and extraction. In *Picture Processing and Psychopictorics*. (Eds) Lipkin, B. and Rosenfeld, A., Academic Press, New York, 75-149, 1970.

Preza, C., Snyder, D.L. and Conchello, J.A. Theoretical development and experimental evaluation of imaging models for differential-interference-contrast microscopy. *Journal of the Optical Society of America A Optics, Image Science, and Vision* 16, 2185-2199, 1999.

R-project, http://www.r-project.org/.

Riddle, D., Blumenthal, T., Meyer, B. and Priess, J. (Eds) *C. ELEGANS II*. Cold Spring Harbor Laboratory Press, New York, 1997.

Schnabel, R., Hutter, H., Moerman, D. and Schnabel, H. Assessing normal embryogenesis in *Caenorhabditis elegans* using a 4D microscope: variability of development and regional specification. *Developmental Biology* 184, 234-265, 1997.

Scott, F.G. *Developmental Biology*. Sinauer Associates, Inc., Massachusetts, 1997.

Sönnichsen, B., Koski, L.B., Walsh, A., Marschall, P., Neumann, B., Brehm, M., Alleaume, A.M., Artelt, J., Bettencourt, P., Cassin, E., Hewitson, M., Holz, C., Khan, M., Lazik, S., Martin, C., Nitzsche, B., Ruer, M., Stamford, J., Winzi, M., Heinkel, R., Roder, M., Finell, J., Hantsch, H., Jones, S.J., Jones, M., Piano, F., Gunsalus, K.C., Oegema, K., Gonczy, P., Coulson, A., Hyman, A.A. and Echeverri, C.J. Full-genome RNAi profiling of early embryogenesis in *Caenorhabditis elegans*. *Nature* 434, 462-469, 2005.

Sterling, T., Savarese, D., Becker, D., Dorband, J., Ranawake, U. and Packer, C. BEOWULF: a parallel workstation for scientific computation. In *Proceedings of the 1995 International Conference on Parallel Processing: August 14-18, 1995, Volume I*. CRC Press, Boca Raton, 11-14, 1995.

Stern, C.D. and Fraser, S.E. Tracing the lineage of tracing cell lineages. *Nature Cell Biology* 3, E216-E218, 2001.

Strome, S., Powers, J., Dunn, M., Reese, K., Malone, C.J., White, J., Seydoux, G. and Saxton, W. Spindle dynamics and the role of gamma-tubulin in early *Caenorhabditis elegans* embryos. *Molecular Biology of the Cell* 12, 1751-1764, 2001.

Sulston, J.E., Schierenberg, E., White, J.G. and Thomson, J.N. The embryonic cell lineage of the nematode *Caenorhabditis elegans*. *Developmental Biology* 100, 64-119, 1983.

Sunderam, V. PVM: a framework for parallel distributed computating. *Concurrency: Practice and Experience* 2, 315-339, 1990.

The *C. elegans* Sequencing Consortium. Genome sequence of the nematode *C. elegans*: a platform for investigating biology. *Science* 282, 2012-2018, 1998.

Thomas, C., DeVries, P., Hardin, J. and White, J. Four-dimensional imaging: computer visualization of 3D movements in living specimens. *Science* 273, 603-607, 1996.

Tuceryan, M. and Jain, A. Texture Analysis. In *The Handbook of Pattern Recognition and Computer Vision*. (Eds) Chen, C., Pau, L. and Wang, P., World Scientific Publishing Co., New Jersey, 207-248, 1998.

Watts, J.L., Etemad-Moghadam, B., Guo, S., Boyd, L., Draper, B.W., Mello, C.C., Priess, J.R. and Kemphues, K.J. *par-6*, a gene involved in the establishment of asymmetry in early *C. elegans* embryos, mediates the asymmetric localization of *PAR-3*. *Development* 122, 3133-3140, 1996.

Welzl, E. Smallest enclosing disks (balls and ellipsoids). *Lecture Notes in Computer Science* 555, 359-370, 1991.

Wood, W. (Ed) *The Nematode Caenorhabditis elegans*. Cold Spring Harbor Laboratory Press, New York, 1988.

Yasuda, T., Bannai, H., Onami, S., Miyano, S. and Kitano, H. Towards Automatic Construction of Cell-Lineage of *C. elegans* from Nomarski DIC Microscope Images. *Genome Informatics* 10, 144-154, 1999.

Yuan, J., Shaham, S., Ledoux, S., Ellis, H.M. and Horvitz, H.R. The *C. elegans* cell death gene *ced-3* encodes a protein similar to mammalian interleukin-1 beta-converting enzyme. *Cell* 75, 641-652, 1993.

Zhang, J., Campbell, R.E., Ting, A.Y. and Tsien, R.Y. Creating new fluorescent probes for cell biology. *Nature Reviews Molecular Cell Biology* 3, 906-918, 2002.